ABSTRACT

Title of Dissertation:	USING VIBRATIONAL SUM-FREQUENCY-GENERATION SPECTROSCOPY TO EXPLORE THE ROLE OF SOLVENT ORGANIZATION IN DETERMINING ION LOCATIONS NEAR SILICA SURFACES
	Siddharth Singh, Doctor of Philosophy, 2024
Dissertation directed by:	Professor John T. Fourkas, Department of Chemistry and Biochemistry

Chemical processes occurring at liquid–solid interfaces are fundamental to applications in fields such as energy storage and nanofluidic transport. In this thesis I establish that the general framework used to describe and understand these systems, the electrical double-layer model, is insufficient in describing interfacial electrolyte solutions in polar, aprotic organic solvents. Using vibrational sum-frequency-generation (VSFG) spectroscopy, a nonlinear optical technique that is indispensable for exploring interfacial organization and dynamics, I study different polar aprotic solvents at silica interfaces. These studies highlight the importance of the organization of such solvents in dictating the interfacial distribution of ions.

In the first part of this dissertation, I compare electrolyte experiments in acetonitrile (MeCN) and propionitrile (EtCN) to determine how an increase in alkyl chain length can influence solvent organization at a liquid–solid (LS) interface, and thereby influence the interactions of ions with the interface. In the second part of the dissertation, I focus on a solvent mixture of EtCN and deuterated MeCN at a silica interface. VSFG data for solutions with different molar ratios of the two solvents indicate that there is preferential partitioning of each liquid at this surface. In the third

part of this dissertation, I examine the effects of solvent chirality on the organizational behavior at an LS interface, and consequently on the effects of this organization on ion partitioning.

The key result of my research is that a polar, aprotic, organic solvent's structure, chirality, and mixing with other solvents, can drive the partitioning of ions in interfacial electrolyte systems, in contradiction to the predictions of the EDL.

USING VIBRATIONAL SUM-FREQUENCY-GENERATION SPECTROSCOPY TO EXPLORE THE ROLE OF SOLVENT ORGANIZATION IN DETERMINING ION LOCATIONS NEAR SILICA SURFACES

by

Siddharth Singh

Dissertation submitted to the Faculty of the Graduate School of the
University of Maryland, College Park, in partial fulfillment
of the requirements for the degree of
Doctor of Philosophy
2024

Advisory Committee:
Professor John T. Fourkas, Chair
Professor Amy Mullin
Professor Pratyush Tiwary
Professor Yu Liu
Professor John Cumings

Dedication

To my parents

Acknowledgements

I would first like to thank my advisor, Prof. John T. Fourkas. When I joined his research group, I did not have any prior experience with LASER sytems, their setup or alignment. Professor Fourkas was extremely patient with and supportive towards me, which allowed me to learn and understand the concepts and experimental skills I needed to complete the research presented here. His depth of scientific knowledge and his ability to explain difficult concepts in simple terms has made it easier for me to navigate my doctoral research journey.

I would next like to thank my committee members: Professor Amy S. Mullin, Professor Pratyush Tiwary, Professor Yu Liu, and Professor John Cumings. I sincerely appreciate their willingness to serve on my committee and provide feedback on my thesis. I would also like to thank Dr. Leah Dodson for being part of my candidacy committee.

Next, I would like to thank former and current group members: Dr. Amanda Souna, Dr. Sandra Gutierrez Razo, Dr. Matt Hourwitz, Dr. Mona Abostate, Dr. Nikos Liaros, Abhishek Kalpattu, Nicholas Fisher, Kishalay Mahato, Ovuokenye Omadoko, Nicholas Lockhart, Arman Hussain, Jeffrey Taylor and Jason Tran. I am lucky to have had such intelligent and humorous labmates. I'm extremely grateful to Dr. Amanda Souna for teaching me the VSFG setup. She has been very helpful and cooperative. She was always willing to help me figure out questions I had regarding concepts of VSFG or alignment of the setup. I am very grateful to Dr. Sandra Gutierrez Razo and Nicholas Fisher for their support and advice in helping resolve not only questions with research but also being friend with whom I could share frustrations with. I would also like to thank Thomas Howard, Dr.Emily Hockey, Darya Kisuryna from the Dodson group and Simone Desouza from the Mullin group for inviting me to events and helping make graduate school fun. They also helped

organize physical chemistry student seminars which were really helpful in learning about research in their groups and in better understanding my own research.

Next, I would like to thank my friends Neha Nanajkar, Dr. Medha Rath, Dr. Lahari Balisetty, Dr. Kyle Webb, Kevin Ramirez, Dr. Leena Pade, Dr. Nilesh Suriyarachchi and Suhas Gotla. Graduate school is difficult and being an international student far away from family makes it even harder. I am lucky to have friends that helped make graduate school a congenial and enjoyable experience. I would especially like to thank Neha for being a kind and considerate friend who is always willing to listen and give good advice.

Most of all, my deepest gratitude and appreciation is to my parents. I genuinely would never have been able to undertake, let alone finish this degree without their constant love and support. They always reassured me when I doubted myself and constantly encouraged me to keep moving forward in my endeavor to complete my research. I am extremely grateful for their faith in me, and I love them very much.

Table of Contents

List of Figures

List of Abbreviations

EtCN Propionitrile

EDL Electrical double layer

FID Free induction decay

FWHM Full width at half maximum

IR Infrared

LBL Lipid bilayer-like

LS Liquid/silica

MeCN Acetonitrile

MeCN-d_3 Deuterated acetonitrile

MD Molecular dynamics

NDFG Noncollinear difference frequency generation

OPA Optical parametric amplifier

PC Propylene carbonate

*rac*PC Racemic propylene carbonate

VSFG Vibrational Sum-frequency generation

Chapter 1: Introduction

Nanoscale science and the drive to understand nanoscale phenomena have gained enormous relevance in recent years, because chemical and biological interactions at the nanoscale play an important role in many applications. These applications range from energy storage devices in the form of batteries,[1,2] and supercapacitors,[3-6] to nanofluidic transport,[7-11] separations based on charged membranes, sensors,[12,13] and biological phenomena such as protein aggregation[14,15] and lipid bilayer permeability.[16,17] A key component of these systems is that electrolyte solutions play a role in self-assembly[18,19] and colloidal stability[20,21] and are used to modulate interactions.

An important thing to note is that moving into the nanoscale regime, bulk properties/interactions are reduced in importance, and interfacial interactions start to dominate. For example, in fluid transport through a nanopore, the fluid experiences significantly greater solid–liquid interactions because the surface-to-volume ratio is orders of magnitude higher than in a bulk system. The asymmetric forces and reduced dimensionality experienced by interfacial liquid molecules make these molecules behave differently fom those in the bulk liquid and affect intermolecular structure and dynamics.[22-27] The nanoscale behavior of electrolyte solutions near interfaces is commonly described using the electrical double-layer (EDL) model [28-29]. The EDL helps describe how the electrical potential depends on the distance from a surface and on the electrolyte concentration. This model is widely used and has proven highly capable in describing the properties of interfacial electrolyte solutions in aqueous systems.

A limitation of the EDL model is that the ions are treated as point charges and the solvent is treated as a homogeneous continuum.[30] Because water as a liquid does not generally exhibit long-range

ordering at interfaces, the continuum solvent description in the EDL model has been highly successful in describing aqueous interfaces. However, for solvents that undergo strong ordering at interfaces, the EDL model has limitations. We have demonstrated that polar aprotic solvents such as acetonitrile (MeCN) and propionitrile (EtCN) show strong ordering at silica interfaces.[31-32] These and other alkyl cyanides are commonly used as solvents, and feature a polar cyano group and a nonpolar alkyl tail. At hydrophilic surfaces, the polar cyano group interacts strongly with the surface charges and can accept hydrogen bonds, whereas the nonpolar groups present mainly an excluded volume region with weak van der Waals attractions. Previous work from our group has shown that at a planar silica surface, MeCN adopts a supported lipid-bilayer-like (LBL) structure consisting of two sublayers with opposite dipole orientations. An interesting feature of this bilayer structure is that it repeats with decreasing fidelity for more than 20 Å from the silica surface. Recently, we have also shown that the thermodynamic stability of this organization is high enough that the structure of the interfacial liquid is essentially unaffected by the presence of lithium perchlorate, even at a concentration of 1 M and that this organization of the solvent dictates the favored positions of the lithium cations and perchlorate anions.[33] We found that at low concentrations of lithium perchlorate the surface potential is negative, but that at higher concentrations the surface potential becomes positive. These results stand in contrast to the predictions of the EDL model, and highlight the need to study and understand the role of solvent organization in determining ion locations near interfaces in polar, aprotic organic solvents.

Having established the requirement to study electrolyte solutions in such solvents and near interfaces, we now need to figure out what methods to use. Buried liquid interfaces are difficult to study experimentally, because such studies require high sensitivity and specificity, as well as

nonvacuum conditions.[34] Spectroscopic techniques such as IR spectroscopy, fluorescence spectroscopy and UV-vis absorption spectroscopy are dominated by contributions from the bulk liquid, and so are not specific enough. Scanning-tunneling microscopy and atomic-force microscopy meet the criteria for sensitivity and specificity, but these methods apply a force to the system, and can only be used readily on thin films of liquids on a solid surface. Other techniques that can be used to study surfaces have large probing depths. X-ray spectroscopy and neutron reflectivity measure regions greater than 1 nm thick, and attenuated total reflection and total internal reflection FTIR spectroscopies measure regions thicker than 100 nm.[35] Second-order non-linear optical (NLO) techniques, on the other hand, have the desired specificity and sensitivity to probe interfacial liquids. Under the electric dipole approximation, second-order NLO techniques are forbidden in media with inversion symmetry, including isotropic bulk media. At the interface between two isotropic media, however, inversion symmetry is broken, and a second-order NLO signal can be observed. Vibrational sum frequency generation (VSFG) spectroscopy is one such second-order NLO technique.

Using VSFG we can probe a region that is one to a few molecular layers thick. The theory behind VSFG spectroscopy was first described in the 1960s by Bloembergen and Pershan.[36] The first successful experiments proving the theory were performed by Shen's group in the 1980s.[37-38] VSFG is now an extremely powerful and essential tool for exploring the molecular organization, interactions, and dynamics that occur at and near interfaces.

In a VSFG experiment, a mid-infrared (IR) laser beam and a visible, or near-infrared, probe laser beam are overlapped spatially and temporally at a sample, generating a signal with a photon energy

equal to the sum of the photon energies of the two incident beams. The signal becomes resonantly enhanced when the mid-IR beam drives a dipole-allowed vibrational transition. The probe beam can be thought of as generating an anti-stokes Raman transition to generate the sum-frequency. By controlling the polarization of the incident and signal beams, information can be obtained regarding the average orientation of molecules at the surface. VSFG spectroscopy can be used to study any interface at which center of symmetry breaks down. These include liquid–solid, gas–solid, liquid–vapor and liquid–liquid interfaces. In this thesis we will focus on liquid/solid interfaces.

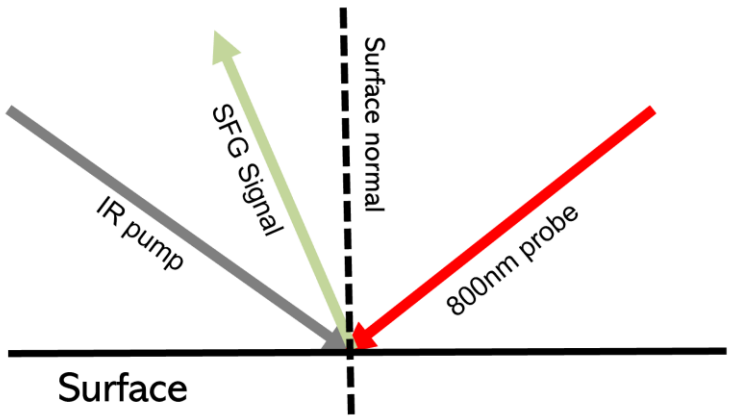

Figure 1.1 Counter-propagating VSFG geometry used for the experiments in this thesis.

If we consider the incident two beams (pump and probe) and the generated beam (SFG signal) to be polarized either parallel, *P*, or perpendicular, *S*, to the plane of incidence and reflection, we can write the polarization configuration of the setup in the order of signal-probe-IR. We can then get orientational information from different configurations. This is because the *SSP* polarization configuration is sensitive to vibrational modes that have a transition dipole moment with a projection along the surface normal, whereas the *SPS* configuration is sensitive to modes that have a transition

dipole moment with a projection along the surface. The *PPP* configuration is sensitive to modes with transition dipole moments in both orientations.

There are different possible implementations of VSFG spectroscopy. The mid-IR source that is used can be broadband or narrowband. Broadband IR pulses, coupled with the development of reliable ultrafast laser sources have increased speed of spectral acquisition. Broadband VSFG also helps eliminate the need to scan through IR wavelengths. [39] The probe source can be continuous-wave or pulsed. Typical probe pulses for frequency-domain experiments are either several picoseconds or more in duration (narrowband), or tens to hundreds of femtoseconds in duration (for time-domain experiments). The superior spectral resolution of the former is required when vibrational modes are closely spaced.[40] Inhomogeneous broadening can be resolved more clearly by time-domain VSFG, also known as free-induction-decay (FID) VSFG, providing insight into time-dependent processes.[41] Incident beams in the experimental setup can be either co- or counter-propagating, and the detection can be performed either in reflected or transmission signal.[42] Transmission geometries are useful when the refractive indices of the two adjacent media are similar,[43] or when there is interference generated by charged interfaces.[44] There are also techniques that involve (phase-sensitive) heterodyne-detection of the signal,[45] or that employ more than two incident beams, such as in pump-SFG-probe experiments.[46] The work I discuss in this thesis has been performed with a homodyne, broadband-IR, narrowband-probe, counter-propagating VSFG setup.[47] The probe pulses are long enough to collect high-resolution spectra. We use VSFG spectroscopy to probe the C-H stretches of liquid molecules, at ~ 2940 cm^{-1}.

The work presented in this thesis is funded by the Centrer for Enhanced Nanofluidic Transport (CENT). CENT is an Energy Frontier Research Center (EFRC) funded by the Department of Energy (DOE). We are working closely with collaborators in CENT who use complimentary

techniques, helping us to build a more detailed understanding of these systems. In particular, I will discuss some work by our collaborator Dr. Zuzanna Siwy and her group at the University of California, Irvine. They use ion-current measurements and other electrochemical techniques to study the same solvent and electrolyte combinations that we do.

Having established the need to explore the role of the organization of polar aprotic organic solvents in determining ion locations near polar surfaces and having introduced the techniques used to study the systems, I will now discuss the solvents to be discussed in this thesis. My work has focused on different polar, aprotic organic solvents, and even combination of these solvents, the understanding of which will help us to draw a more general picture of the interfacial organization of these solvents and its effects on the locations of ions.

The first solvent I discuss here is EtCN. EtCN-based electrolytes exhibit a large and symmetric electrochemical stability, an exceptional anodic potential limit, good ionic conductivity, and low viscosity. [48] For this reason EtCN is used in mixtures as a solvent in lithium-ion batteries. We have chosen to study EtCN in our work to compare the interaction of ionic salts between this liquid and MeCN. We have seen in our previous studies that EtCN forms LBL structures to that are similar to those of MeCN at silica interface.[49] Longer chains in alkyl cyanides introduce additional steric hindrance and packing constraints that can influence intermolecular ordering at interfaces. EtCN has an extra methylene group as compared with MeCN, and the methyl group in EtCN is angled away from the CN head orientation. These structural features increase the volume and change the shape of the nonpolar region of the molecule, which influenced the intermolecular ordering of this liquid at polar interfaces. At the same time, increasing the length of the alkyl tail changes the

balance between polar and dispersive interactions among the liquid molecules, which can also impact intermolecular structure and dynamics at interfaces.

We have also studied solvent mixtures at silica interfaces and how these combinations affect the molecular organization. These experiments are relevant because a mixture of solvents is often used in lithium-ion batteries. Generally, solvents in lithium-ion batteries use a mixture of ethylene carbonate (EC) and some linear organic carbonates such as ethyl methyl carbonate (EMC), diethyl carbonate (DEC), or dimethyl carbonate (DMC) with $LiPF_6$ as the electrolyte. The presence of EC leads to an increase in the viscosity of the solution, which in turn lowers the conductivity compared to EC-free electrolytes, especially at low temperatures. The conductivity can still be improved to some extent by using higher weight fractions of low-viscosity, linear-carbonate-based co-solvents.[51] However, because EC has desirable characteristics as a aprotic polar organic solvent, researchers have used EC in combination with other solvents to make it a solvent that is liquid at room temperature.[50] This mixing, however, can lead to different organizational behavior among solvents at interfaces, as I will show in this thesis.

I have used a combination of EtCN and deuterated MeCN (MeCN-d_3) to model such a system. MeCN-d_3, is an isotopically enriched solvent that is widely used in high resolution NMR studies due to its high chemical and isotopic purity. We use MeCN-d_3 so that we do not have a peak in our VSFG spectra for symmetric the C-H stretching frequency of MeCN complicating our EtCN spectra. Another solvent I have studied is propylene carbonate (PC). PC is commonly used as a polar, aprotic solvent.[52]

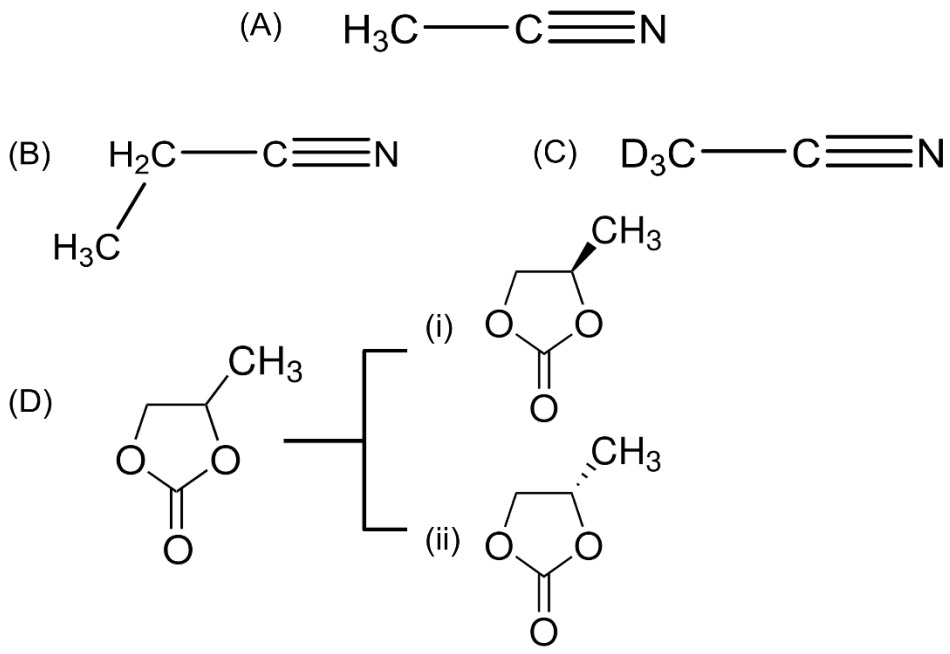

Figure 1.2 Solvents used in this thesis. (A) Acetonitrile (MeCN), (B) Propionitrile (EtCN), (C) Deuterated acetonitrile (MeCN-d_3), (D)Propylene Carbonate (PC), (D(i)) R-Propylene carbonate, (D(ii)) S-Propylene carbonate

PC has a dipole moment of 4.9 D, which is considerably higher than those of, for instance, acetone (2.91 D) and ethyl acetate (1.78 D). Due to PC's high relative permittivity (dielectric constant) of ε=64, this solvent is frequently used as a high-permittivity component of electrolyte solutions in lithium batteries, usually together with a low-viscosity solvent (e.g. dimethoxy ethane). PC's high polarity allows this solvent to create an effective solvation shell around lithium ions, thereby creating a conductive electrolyte. PC can also be found in some adhesives, paint strippers, and cosmetics. An interesting feature of PC is that it is a chiral molecule. The *R* and *S* enantiomers of PC are two compounds with the exact same connectivity, but that are mirror images of each other. This feature intrigues us, and we wanted to see if chirality could play a role in the organization of

the PC at silica interface, potentially leading to an effect on the preferred ion locations at the interface.

1.2 Outline

The goal of the work described in this thesis is to develop insights into the solvent–silica interface, and specifically polar, aprotic organic solvents, for applications such as separations, heterogeneous catalysis, nanofluidics, and energy storage.

The outline of this thesis is as follows:

- Chapter Two: The counter propagating, broadband VSFG spectrometer employed for all experiments presented in this thesis is discussed.
- Chapter Three: I discuss the VSFG spectra of $LiClO_4$ salts in EtCN at the silica interface, and compare the spectra to those for MeCN at the same interface. We observe that ions can partition into the surface bilayer at lower electrolyte concentrations in EtCN compared to MeCN
- Chapter Four: I present VSFG results for a mixture of MeCN-d_3 and EtCN at a silica interface. I studied this combination of solvents to gain a deeper insight into the bilayer organization of the solvents, and if and how that organization is affected due to the presence of two different molecules and the interactions between them. My results show a clear sign of preferential partitioning of the individual solvents to one of the sublayers of the surface bilayer.
- Chapter Five: I compare VSFG spectra of racemic PC to those of its pure enantiomers and use these results to gain insights into the organization of this solvent at the silica interface,

and into whether chirality causes a difference in the organization. I also consider the effect the chirality has on how ions partition at the silica surface. My results show that racemic propylene carbonate creates a layered structure at the silica interface that is more ordered than the enantiomeric one.

- Chapter Six: I discuss the VSFG spectra of $LiClO_4$ salts in racemic and R-enantiomeric PC at the silica interface. Our experiments reveal that the possible additional free volume in (*R*)-PC in comparison to *rac*PC enables ions to penetrate the surface bilayer in the former liquid even at very low electrolyte concentrations. Experiments from our collaborators indicate that differences in the packing density of *rac*PC and (*R*)-PC lead to strikingly different electrochemical and electrokinetic behavior at a polar interface.
- Chapter Seven: Conclusions and future work

1.3 References

(1) Zhang, S. S. A Review on Electrolyte Additives for Lithium-Ion Batteries. *J. Power Sources* **2006**, *162* (2), 1379–1394.

(2) Aurbach, D.; Talyosef, Y.; Markovsky, B.; Markevich, E.; Zinigrad, E.; Asraf, L.; Gnanaraj, J. S.; Kim, H.-J. Design of Electrolyte Solutions for Li and Li-Ion Batteries: A Review. *Electrochem. Acta* **2004**, *50* (2–3), 247–254.

(3) Bhat, T. S.; Patil, P. S.; Rakhi, R. B. Recent Trends in Electrolytes for Supercapacitors. *J. Energy Storage* **2022**, *50* (104222), 104222.

(4) Zhong, C.; Deng, Y.; Hu, W.; Qiao, J.; Zhang, L.; Zhang, J. A Review of Electrolyte Materials and Compositions for Electrochemical Supercapacitors. *Chem. Soc. Rev.* **2015**, *44* (21), 7484–7539.

(5) Bu, F.; Zhou, W.; Xu, Y.; Du, Y.; Guan, C.; Huang, W. Recent Developments of Advanced Micro-Supercapacitors: Design, Fabrication and Applications. *Npj Flex. Electron.* **2020**, *4* (1), 1–16.

(6) Poonam; Sharma, K.; Arora, A.; Tripathi, S. K. Review of Supercapacitors: Materials and Devices. *J. Energy Storage* **2019**, *21*, 801–825.

(7) Schoch, R. B.; Han, J.; Renaud, P. Transport Phenomena in Nanofluidics. *Rev. Mod. Phys.* **2008**, *80* (3), 839–883.

(8) Vlassiouk, I.; Smirnov, S.; Siwy, Z. Ionic Selectivity of Single Nanochannels. *Nano Lett.* **2008**, *8* (7), 1978–1985.

(9) White, H. S.; Bund, A. Ion Current Rectification at Nanopores in Glass Membranes. *Langmuir* **2008**, *24* (5), 2212–2218.

(10) Cervera, J.; Schiedt, B.; Ramírez, P. A Poisson/Nernst-Planck Model for Ionic Transport through Synthetic Conical Nanopores. *EPL* **2005**, *71* (1), 35–41.

(11) Siwy, Z. S.; Howorka, S. Engineered Voltage-Responsive Nanopores. *Chem. Soc. Rev.* **2010**, *39* (3), 1115–1132.

(12) Munje, R. D.; Muthukumar, S.; Panneer Selvam, A.; Prasad, S. Flexible Nanoporous Tunable Electrical Double Layer Biosensors for Sweat Diagnostics. *Sci. Rep.* **2015**, *5* (1), 1–11.

(13) Smeets, R. M. M.; Keyser, U. F.; Krapf, D.; Wu, M.-Y.; Dekker, N. H.; Dekker, C. Salt Dependence of Ion Transport and DNA Translocation through Solid-State Nanopores. *Nano Lett.* **2006**, *6* (1), 89–95.

(14) Roberts, D.; Keeling, R.; Tracka, M.; van der Walle, C. F.; Uddin, S.; Warwicker, J.; Curtis, R. The Role of Electrostatics in Protein–Protein Interactions of a Monoclonal Antibody. *Mol. Pharm.* **2014**, *11* (7), 2475–2489.

(15) Zhang, J.; Liu, X. Y. Effect of Protein–Protein Interactions on Protein Aggregation Kinetics. *J. Chem. Phys.* **2003**, *119* (20), 10972–10976.

(16) Macdonald, R. C.; Bangham, A. D. Comparison of Double Layer Potentials in Lipid Monolayers and Lipid Bilayer Membranes. *J. Membr. Biol.* **1972**, *7* (1), 29–53.

(17) Sinha, S.; Sachar, H. S.; Das, S. Effect of Plasma Membrane Semipermeability in Making the Membrane Electric Double Layer Capacitances Significant. *Langmuir* **2018**, *34* (4), 1760–1766.

(18) Leontidis, E. Hofmeister Anion Effects on Surfactant Self-Assembly and the Formation of Mesoporous Solids. *Curr. Opin. Colloid Interface Sci.* **2002**, *7* (1–2), 81–91.

(19) Edel, J. B.; Kornyshev, A. A.; Kucernak, A. R.; Urbakh, M. Fundamentals and Applications of Self-Assembled Plasmonic Nanoparticles at Interfaces. *Chem. Soc. Rev.* **2016**, *45* (6), 1581–1596.

(20) Trefalt, G.; Szilagyi, I.; Téllez, G.; Borkovec, M. Colloidal Stability in Asymmetric Electrolytes: Modifications of the Schulze–Hardy Rule. *Langmuir* **2017**, *33* (7), 1695–1704.

(21) Lyklema, J. Principles of Interactions in Non-Aqueous Electrolyte Solutions. *Curr. Opin. Colloid Interface Sci.* **2013**, *18* (2), 116–128.

(22) Benjamin, I. Molecular Structure and Dynamics at Liquid-Liquid Interfaces. *Annu. Rev.Phys.Chem.***1997**,*48*(1), 407–451.

(23) Penfold, J. The Structure of the Surface of Pure Liquids. *Rep. Prog. Phys.* **2001**, *64* (7), 777–814.

(24) Weeks, J. D. CONNECTING LOCAL STRUCTURE TO INTERFACE FORMATION: A Molecular Scale van Der Waals Theory of Nonuniform Liquids. *Annu. Rev. Phys. Chem.* **2002**, *53* (1), 533–562.

(25) Nathanson, G. M. Molecular Beam Studies of Gas-Liquid Interfaces. *Annu. Rev. Phys. Chem.* **2004**, *55* (1), 231–255.

(26) Kaplan, W. D.; Kauffmann, Y. Structural Order in Liquids Induced by Interfaces with Crystals. *Annu. Rev. Mater. Res.* **2006**, *36* (1), 1–48.

(27) Moore, F. G.; Richmond, G. L. Integration or Segregation: How Do Molecules Behave at Oil/Water Interfaces? *Acc. Chem. Res.* **2008**, *41* (6), 739–748.

(28) Israelachvili, J. N. *Intermolecular and Surface Forces*, 3rd ed.; Academic Press: San Diego, CA, 2017.

(29) Wu, J. Understanding the Electric Double-Layer Structure, Capacitance, and Charging Dynamics. *Chem. Rev.* **2022**, *122* (12), 10821–10859.

(30) Trasatti, S. Relative and Absolute Electrochemical Quantities. Components of the Potential Difference across the Electrode/Solution Interface. *J. Chem. Soc.* **1974**, *70* (0), 1752.

(31) Ding, F.; Hu, Z.; Zhong, Q.; Manfred, K.; Gattass, R. R.; Brindza, M. R.; Fourkas, J. T.; Walker, R. A.; Weeks, J. D. Interfacial Organization of Acetonitrile: Simulation and Experiment. *J. Phys. Chem. C Nanomater. Interfaces* **2010**, *114* (41), 17651–17659.

(32) Liu, S.; Hu, Z.; Weeks, J. D.; Fourkas, J. T. Structure of Liquid Propionitrile at Interfaces. 1. Molecular Dynamics Simulations. *J. Phys. Chem. C Nanomater. Interfaces* **2012**, *116* (6), 4012–4018.

(33) Polster, J. W.; Souna, A. J.; Motevaselian, M. H.; Lucas, R. A.; Tran, J. D.; Siwy, Z. S.; Aluru, N. R.; Fourkas, J. T. The Electrical-double Layer Revisited. *Nat. Sci. (Weinh.)* **2022**, *2* (2).

(34) Buck, M.; Himmelhaus, M., Vibrational spectroscopy of interfaces by infrared-visible sum frequency generation. *J. Vac. Sci. Technol. A* **2001,** *19* (6), 2717-2736.

(35) Shen, Y. R.; Ostroverkhov, V., Sum-frequency vibrational spectroscopy on water interfaces: Polar orientation of water molecules at interfaces. *Chem. Rev.* **2006,** *106* (4), 1140-1154.

(36). Bloembergen, N.; Pershan, P. S., Light waves at the boundary of nonlinear media *Phys. Rev.* **1962,** *128* (2), 606-&.

(37) Hunt, J. H.; Guyotsionnest, P.; Shen, Y. R., Observation of C-H stretch vibrations of monolayers of molecules. Optical sum-frequency generation. *Chem. Phys. Lett.* **1987,** *133* (3), 189-192. 15

(38) Zhu, X. D.; Suhr, H.; Shen, Y. R., Surface vibrational spectroscopy by infrared-visible sum frequency generation *Phys. Rev. B* **1987,** *35* (6), 3047-3050.

(39) Richter, L. J.; Petralli-Mallow, T. P.; Stephenson, J. C., Vibrationally resolved sum-frequency generation with broad-bandwidth infrared pulses. *Opt. Lett.* **1998,** *23* (20), 1594-1596.

(40) Wang, H. F.; Velarde, L.; Gan, W.; Fu, L., Quantitative sum-frequency generation vibrational spectroscopy of molecular surfaces and interfaces: lineshape, polarization, and orientation. *Annu. Rev. Phys. Chem.* **2015,** *66*, 189-216.

(41) Bonn, M.; Ueba, H.; Wolf, M., Theory of sum-frequency generation spectroscopy of adsorbed molecules using the density matrix method—broadband vibrational sum-frequency generation and applications. *J. Phys.-Condens. Mat.* **2005,** *17*, S201-S220.

(42) Dick, B.; Gierulski, A.; Marowsky, G.; Reider, G. A., Determination of the nonlinear optical susceptibility of surface layers by sum and difference frequency generation in reflection and transmission. *Appl. Phys. B-Photo.* **1985,** *38* (2), 107-116.

(43) Messmer, M. C.; Conboy, J. C.; Richmond, G. L., Observation of molecular ordering at the liquid-liquid interface by resonant sum-frequency generation. *J. Am. Chem. Soc.* **1995,** *117* (30), 8039-8040.

(44) Gonella, G.; Lütgebaucks, C.; de Beer, A. G. F.; Roke, S., Second harmonic and sum-frequency generation from aqueous interfaces is modulated by interference. *J. Phys. Chem. C* **2016,** *120* (17), 9165-9173.

(45) Shen, Y. R., Phase-sensitive sum-frequency spectroscopy. *Annu. Rev. Phys. Chem.* **2013,** *64*, 129-50.

(46) Ghosh, A.; Smits, M.; Bredenbeck, J.; Dijkhuizen, N.; Bonn, M., Femtosecond time-resolved and two-dimensional vibrational sum frequency spectroscopic instrumentation to study structural dynamics at interfaces. *Rev. Sci. Instrum.* **2008,** *79* (9).

(47) Ding, F.; Zhong, Q.; Brindza, M. R.; Fourkas, J. T.; Walker, R. A., Ti:sapphire, broadband vibrational sum-frequency generation spectrometer with a counter-propagating geometry. *Optics Exp.* **2009,** *17*, 14665-75.

(48) Nguyen, H. V. T.; Faheem, A. B.; Kwak, K.; Lee, K.-K. Propionitrile as a Single Organic Solvent for High Voltage Electric Double-Layer Capacitors. *J. Power Sources* **2020**, *463* (228134), 228134.

(49) Ding, F.; Zhong, Q.; Manfred, K.; He, X.; Bender, J. S.; Brindza, M. R.; Walker, R. A.; Fourkas, J. T. Structure of Liquid Propionitrile at Interfaces. 2. Experiment. *J. Phys. Chem. C Nanomater. Interfaces* **2012**, *116* (6), 4019–4025.

(50) Petibon, R.; Harlow, J.; Le, D. B.; Dahn, J. R. The Use of Ethyl Acetate and Methyl Propanoate in Combination with Vinylene Carbonate as Ethylene Carbonate-Free Solvent Blends for Electrolytes in Li-Ion Batteries. *Electrochim. Acta* **2015**, *154*, 227–234.

(51) Smart, M. C.; Ratnakumar, B. V.; Surampudi, S. Electrolytes for Low-temperature Lithium Batteries Based on Ternary Mixtures of Aliphatic Carbonates. *J. Electrochem. Soc.* **1999**, *146* (2), 486–492.

(52) Stoye, D. Solvents. *Ullmann's Encyclopedia of Industrial Chemistry*. Wiley June 15, 2000. https://doi.org/10.1002/14356007.a24_437.

(53) *Propylene Carbonate Solvent Properties*. Lsu.edu.

Chapter 2: Experimental Setup

2.1. Setup and alignment

The experiments described in this dissertation are conducted using a broadband, counter-propagating, VSFG spectrometer. The broadband approach uses a high bandwidth (~250 cm^{-1}) IR pulse, allowing for fast data acquisition by eliminating the need to scan over many IR wavelengths. This broadband approach is similar to the one used by Richter and coworkers.[1] The two beams for the sum-frequency-generation approach used here, reach the sample in a counter-propagating geometry. We chose this scheme because, unlike in the copropagating geometry, there is a large angular separation of the VSFG signal from the reflected visible beam, which helps to prevent the input visible light from reaching the detector. The counter-propagating geometry also provides more space in the sample area, making adjustment of optics convenient. We have found that the counter-propagating geometry can provide substantial improvement in the signal-to-noise ratio and minimize any signal from the bulk.[2]

A schematic of our VSFG experimental apparatus is shown in Figure 2.1. We start with 5.2-W, continuous wave, 532-nm (Coherent Verdi-12) Nd:YAG laser that pumps a 76-MHz, mode-locked Ti-sapphire oscillator (Coherent Mira) that operates at 800nm. This oscillator in turn seeds a 1-kHz, Ti-sapphire regenerative amplifier (Coherent Legend Elite), which generates 3 W of 800-nm, 80-fs pulses. The amplifier is pumped with a Q-switched, frequency-doubled, neodymium-doped yttrium lithium fluoride (Nd:YLF), 1 kHz, 532-nm (Coherent Evolution) laser. This amplifier output acts as the light source for the VSFG experiments. The Mira output is modified with a pulse shaper before entering the amplifier, to help ensure nearly transform-limited IR pulses at the sample.[3]

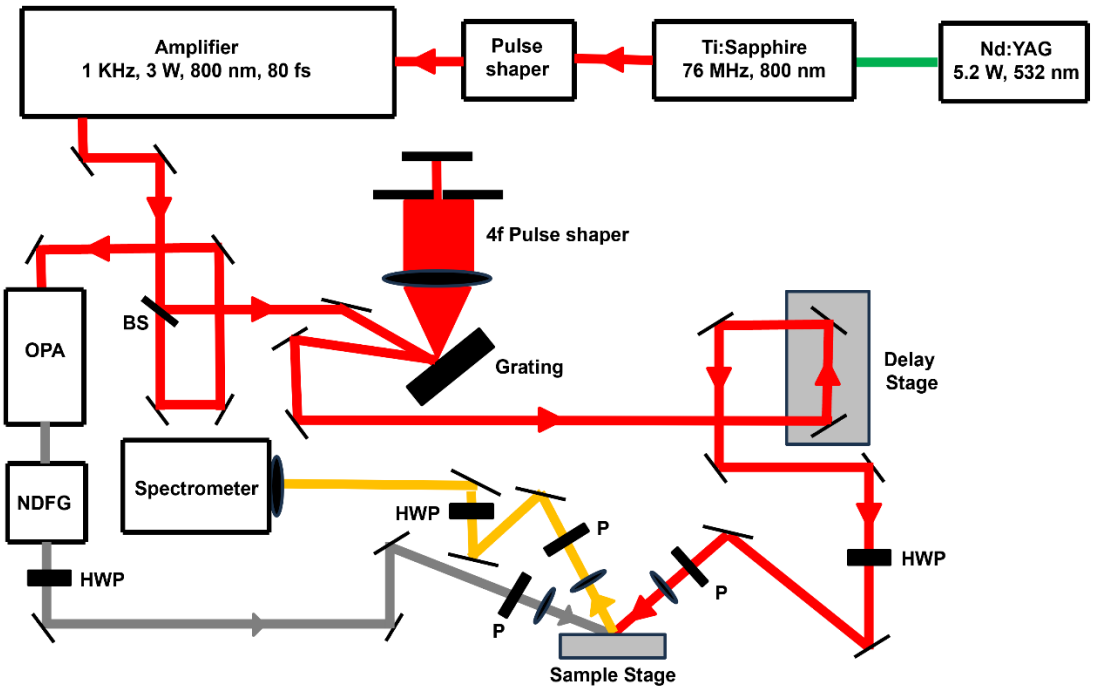

Figure 2.1 Schematic of VSFG spectrometer. BS = beam splitter; HWP = half-wave plate; P = polarizer. Beam frequency is indicated as follows: green = 532 nm; red = 800 nm; grey = mid-IR (~3000 cm-1); and yellow = sum frequency (~ 650 nm).

The amplifier output is directed through a 30/70 beam splitter, after which 30% of the power is sent along the mid-IR generating pump path and the 70% along the 800-nm probe path. The mid-IR pulses are generated with an optical parametric amplifier (OPA) and a noncollinear difference frequency generation (NDFG) module (TOPAS, Light Conversion) and have an average power of ~15 mW. The IR wavelength is tuned with the WinTOPAS software, which controls the rotation of three nonlinear crystals, the translation of delay stages to control temporal overlap, and the orientation of a mirror that improves overlap between the signal and idler beam at the NDFG

crystal. The NDFG output passes through a half-wave plate and a polarizer that control the polarization of the beam at the sample.

The probe pulse is first sent to a 4*f*-pulse shaper to help selects a narrow portion (4-10 cm^{-1}) of the 800-nm spectrum. The pulse shaper uses a grating (1800 lines/mm, Spectrogon) and a movable slit. After the pulse shaper the probe pulse passes down a motorized delay stage that helps control the temporal overlap of the probe and pump pulses at the sample. After the delay stage, the probe beam passes through a half-wave plate and polarizer to help control its polarization at the sample.

The angles of incidence of the IR and probe beams are -58^o and 61^o from the surface normal, respectively (Figure 2.2.) A negative angle designates an angle directed to the left of the surface normal. By utilizing the phase-matching condition, we are able to calculate that the sum-frequency signal is generated at an angle of -32.8^o from the sample surface. This generated sum-frequency signal is then sent to a spectrometer after passing through a polarizer and half-wave plate. The polarizer helps select the polarization of the beam, and the half-wave plate ensures that the light is always *S*-polarized when entering the spectrometer, as the gratings are polarization-sensitive. The signal is directed through the entrance slit of the spectrometer (Acton, SP2300i) and detected with a 100 × 1340 pixel CCD array (Spec-10:100, Roper Science) with a resolution of 0.02 nm/pixel.

To optimize and align the pump beam we make adjustments to optics in the first and second pass of the OPA and in the NDFG module to maximize power and bandwidth. A white- light continuum is generated by focusing a small portion of the 800-nm beam through a sapphire plate in the first pass of the OPA. The white-light continuum quality is improved by optimizing pulse compression

in the amplifier by adjusting a motorized mirror. The spatial and temporal overlap are then adjusted at each of the nonlinear crystals: the first and second pass of the OPA and the $AgGaS_2$ crystal in the NDFG module. In the first pass of the OPA, and in the NDFG unit, the beams overlap noncollinearly, and therefore the interacting beams must be at the optimal angles.

Once an IR signal is generated it is optimized using a WinTOPAS software, which utilizes motorized optics to improve the signal. The IR beam is then overlayed with a HeNe tracer beam to facilitate alignment into the sample.

To overlap the IR and probe pulses at the sample spatially and temporally, a ZnSe substrate is used. The focused IR and 800-nm beams each generate blue luminescence that is overlapped. Once spatial overlap is achieved, temporal overlap is found by changing the path length of the 800-nm beam in ~150 fs increments using a motorized delay stage, until an orange glow is observed coming from the ZnSe. The orange light is then focused and directed into the entrance slit of the spectrometer. The alignment and overlap are fine-tuned by replacing the ZnSe with a gold substrate, the surface of which generates a strong nonresonant SFG response. The gold spectrum is also to normalize sample spectra. The nonresonant response is independent of wavelength in the methyl stretch region, and the VSFG signal is therefore proportional to the IR intensity only. A gold spectrum is therefore representative of the spectrum of the IR pulse, which eliminates the need to measure this spectrum directly.[3] If the vibrational modes of interest are far apart in energy, the IR wavelength can be tuned in increments of 50-100 cm^{-1} over whatever range necessary. A gold VSFG spectrum is collected at each of these wavelength settings. Calibration is performed by placing a thin sheet of polystyrene in the path of the IR beam while collecting a gold spectrum, as shown in Figure 2.2.

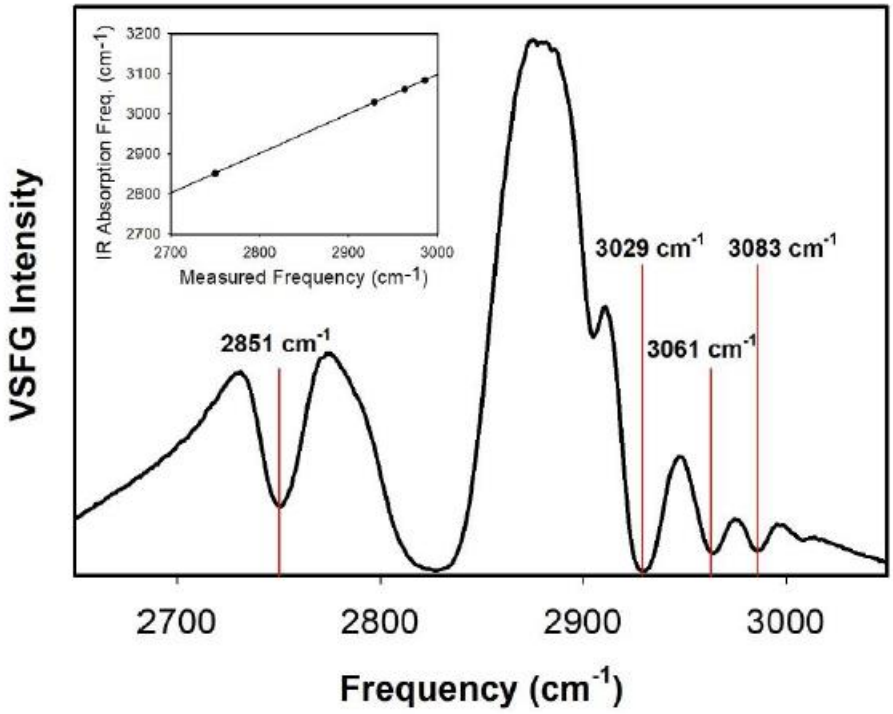

Figure 2.2. Nonresonant VSFG spectrum from gold substrate with a polystyrene film placed in the IR path. The red lines indicate the four peaks used to calibrate the VSFG spectra. The inset indicates the expected linear relationship between the measured frequency and the IR absorption peaks for polystyrene. (The 800-nm probe frequency has been subtracted from the actual measured frequency values to arrive at the frequencies for the *x*-axes)[(6)].

To effectively generate a VSFG signal, both IR and probe pulses should be near the transform limit. We can generate a nearly transform-limited pulse by utilizing a pulse shaping procedure using multiphoton intrapulse interference phase scan (MIIPS) software.[4] The unstretched probe pulse (with the slit removed) is focused through a barium borate crystal positioned within several centimeters of the sample stage to generate 400-nm light. The 400-nm spectrum is collected with a fiber-optic cable and analyzed by the MIIPS software in real time. The software compares the

800-nm spectrum to the 400-nm spectrum and simultaneously adjusts the phase of each frequency component of the seed pulse using a grating and a spatial light modulator positioned immediately before the amplifier. Prior to performing sample scans, the delay between the IR and probe pulses is adjusted to optimize the overlap between the molecular response generated by the IR and the electric fields probe.[5] This optimization is accomplished using the delay stage on the probe pathway. The sample stage height is also adjusted in increments of approximately 6 μm while maximizing the intensity of the gold signal.

2.2. Data collection and analysis

When starting to collect data we first measure the background signal by blocking the IR beam. The acquisition time for the background signal is equal to that used for the VSFG experiment. The background spectrum is subtracted automatically from any subsequent sample scan by our data collection software. Sample scans are repeated at least three times, with an acquisition time that depends on the strength of the signal. This time is generally in the range of 30-480 s. All spectra are calibrated and normalized using a LabVIEW program. Four absorption lines are selected from the polystyrene calibration spectrum, as shown in Figure 2.2. We also use a normalization range for the data compared to the gold spectrum at each wavelength, only selecting data points with greater than a threshold of 10,000 counts, relative to a noise level of ~30 counts. All sample scans are calculated together before normalizing and calibrating.

2.3 References

1. Richter, L. J.; Petralli-Mallow, T. P.; Stephenson, J. C., Vibrationally resolved sum-frequency generation with broad-bandwidth infrared pulses. *Opt. Lett.* **1998,** *23* (20), 1594-1596.

2. Ding, F.; Zhong, Q.; Brindza, M. R.; Fourkas, J. T.; Walker, R. A., Ti:sapphire, broadband vibrational sum-frequency generation spectrometer with a counter-propagating geometry. *Opt. Express* **2009,** *17* (17), 14665-14675.

3. Liebsch, A., Theory of sum frequency generation from metal surfaces. *Appl. Phys. B-Lasers O.* **1999,** *68*, 301-304.

4. Lozovoy, V. V.; Pastirk, I.; Dantus, M., Multiphoton intrapulse interference. IV. Ultrashort laser pulse spectral phase characterization and compensation. *Opt. Lett.* **2004,** *29*,
775-7.

5. Stiopkin, I. V.; Jayathilake, H. D.; Weeraman, C.; Benderskii, A. V., Temporal effects on spectroscopic line shapes, resolution, and sensitivity of the broad-band sum frequency generation. *J. Chem. Phys.* **2010,** *132*, 234503.

6. Souna, A.J; Thesis 'The liquid acetonitrile/silica interface: A model system for reinterpreting the vibrational sum-frequency generation (VSFG) spectra of liquid/solid interfaces', **2018,** UMD

Chapter 3: VSFG studies of $LiClO_4$ in propionitrile at the silica interface

VSFG spectroscopy research conducted by: Siddharth Singh
Electrolyte solutions prepared by: Ovuokenye Omadoko

3.1 Introduction

Understanding the surface electrostatic potential is of critical importance, as this potential is widely applied in describing transport phenomena in nanofludics,[1-5] separations based on charged membranes,[6,7] electrokinetic effects,[8] energy–storage devices such as supercapacitors,[9,10] sensors,[11,12] and biological phenomena such as protein aggregation[13,14] and lipid–bilayer permeability.[15] The surface electrostatic potential between ions and a charged or polar surface is called the electrical-double layer (EDL) model. This model consists of a charged surface in contact with a liquid region with an enhanced concentration of counterions.[16] In this model, the ionic distribution near an interface is frequently described by the Poisson–Boltzmann equation,[17] which treats the ions as point charges and the solvent as a homogeneous dielectric continuum. The continuum solvent description in the EDL model has been highly successful in modeling aqueous interfaces, because water does not generally exhibit long-range ordering at interfaces, although short-range organization (on the order of two molecular diameters) is observed.[18-19]

The continuum description is insufficient for solvents that undergo strong ordering at interfaces.[19,20] For example, acetonitrile forms a well-ordered, lipid-bilayer-like organization at silica interfaces.[21] The bilayer consists of a first sub-layer of molecules in which the cyano groups accept hydrogen bonds from surface silanol groups, and a second, interdigitated layer of molecules that predominantly point in the opposite direction.[22-24] This bilayer organization repeats with decreasing fidelity for more than 2 nm from the silica surface.[22] Our group has

shown previously that because of this bilayer organization in acetonitrile, the surface potential between ions and a silica surface is different than that in an aqueous system.[26-27] In an aqueous system, the silica surface is negatively charged due to deprotonation of silanol groups. This negative charge determines the distribution of ions in the interfacial solution. However, in the silica–liquid acetonitrile system, the interface can exhibit either a negative or a positive charge, depending on the concentration and identity of the salt. Because the silica surface remains uncharged but polar, the acetonitrile organizes in a manner that resembles a thermodynamically stable, supported lipid bilayer. We had found that this ordering is remarkably insensitive to the presence of ions, even at concentrations of 1M and above. Because of this organization, the polarity and magnitude of the effective surface potential depend on the electrolyte concentration and the identities of the anion and cation. The layered solvent structure was found to modify ionic distributions over length scales and concentrations that are substantially larger than predicted by the classical EDL picture.

In the present work explore whether this deviation from the EDL picture is present in polar aprotic organic solvents other than MeCN. We used propionitrile because we have shown in previous work that this liquid forms a bilayer at the silica interface that is similar to that of MeCN.[22] EtCN has an extra methylene group as compared with MeCN, and the methyl group in EtCN is angled away from the CN head orientation. These effects cause EtCN to exhibit a more compact bilayer as compared to MeCN.(REF) These structural features also increase the volume and change the shape of the nonpolar region of the molecule, which is expected to influence the intermolecular ordering of EtCN at interfaces. We wished to explore whether these differences in the solvent organization affect the interactions of the solvent and the ions, and contrast the results to those for MeCN.

3.2 Methods

The details of our counterpropagating VSFG spectrometer were given in Chapter 2. For the studies reported here the probe bandwidth was narrowed to ~5 cm^{-1}. The probe spectrum used for the experiments reported here was centered at 800 nm. For this study we used the *SSP* polarization configuration. At the sample, the probe pulse energy was ~15 μJ, and the IR pulse energy was 14 μJ. The sample consisted of 99+% spectroscopic grade EtCN (SigmaAldrich). The $LiClO_4$ was ≥99.99% battery grade (Sigma Aldrich). $LiClO_4$ came in a sealed ampoule and was used as received without further drying. The electrolyte solutions had concentrations that ranged from 1 nM to 1 M. A neat EtCN sample was also prepared as a control. The samples were held in an IR-grade quartz cell with a 1-mm path length (FireflySci). The cell was rinsed, oven-dried, and oxygen-plasma cleaned immediately prior to use. Acquisition times for low concentrations of electrolyte solutions were 30 s. For higher concentrations, acquisition times were two to four times those at low concentrations, depending on the signal strength. All scans were repeated at least five times.

3.3 Results and Discussion

We obtained VSFG spectra of neat EtCN before starting with the electrolyte experiments. As is the case for MeCN, EtCN has strong VSFG signal, in the C–H stretching region because the cyano group in the first sublayer interacts with the –OH group from the silica surface, but not in the second sublayer. The stretching frequencies of the methyl group in MeCN, and the methylene group in EtCN are different in the two sublayers, causing asymmetry. Hence strong signal is achieved. The peak for these stretches occurs at ~ 2940 cm^{-1} in EtCN,as seen in Fig 3.1.

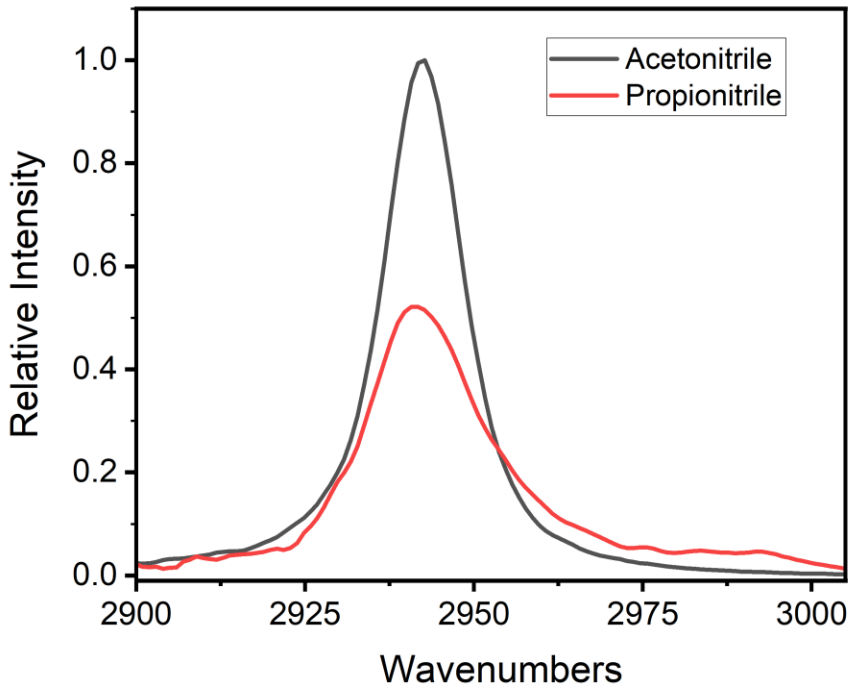

Figure 3.1. VSFG spectra of neat MeCN and EtCN in the C–H stretching region.

Comparing the neat EtCN signal to the neat MeCN signal, we see that it is less intense the signal in the former liquid. This behavior is expected, because the methyl group in the MeCN has three hydrogens compared to the two in the methylene group of the EtCN. We would therefore predict, to first approximation, that MeCN should have a signal that is $(3/2)^2$ times as strong as that of EtCN. The data agree reasonably well with this prediction. It should be noted as well that there is a stronger asymmetric stretch signal in EtCN, because the methylene group is not a freee rotor. The resultant tail to the blue of the peak increases the overall intensity.

Another peak that can appear in the VSFG spectra for EtCN, is the methyl symmetric stretch, at ~ 2890 cm^{-1}. We do not observe this peak in neat EtCN at the silica interface, because the

methyl stretch frequency is not shifted in the second sublayer of the bilayer compared to the first sublayer. The relative centrosymmetry of the bilayer leads to the disappearance of the symmetric stretch peak.

We next consider electrolyte solution in EtCN at the silica interface. To help compare the data to MeCN results published previously, we used the same salt, $LiClO_4$. Electrochemical devices such as batteries often make use of lithium-based electrolytes, with the requirement that lithium ions be highly mobile and have a stable and inert counterion.[2]

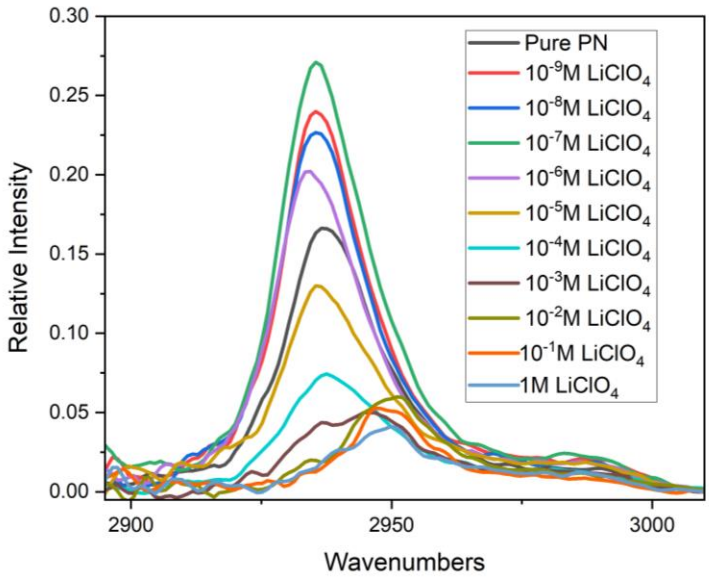

Figure.3.2. VSFG spectra of $LiClO_4$ in propionitrile at a silica interface. The spectra were measured in the C–H symmetric stretch region.

The VSFG data in Figure 3.2 show similar behavior to that seen for MeCN. The VSFG increases in signal intensity at low $LiClO_4$ concentrations reaches a maximum, and then decreases by an order of magnitude from its peak value.

The key features of the concentration dependent VSFG spectra are quantified in Figures 3.3-3.5. Fig.3.3. shows that the peak intensities of $LiClO_4$ in MeCN and EtCN, relative to the peak intensity of the respective neat samples, behave differently with increasing concentration. The highest relative intensity in EtCN is around 1.4 times that in the neat liquid whereas in MeCN this ratio is 1.1.

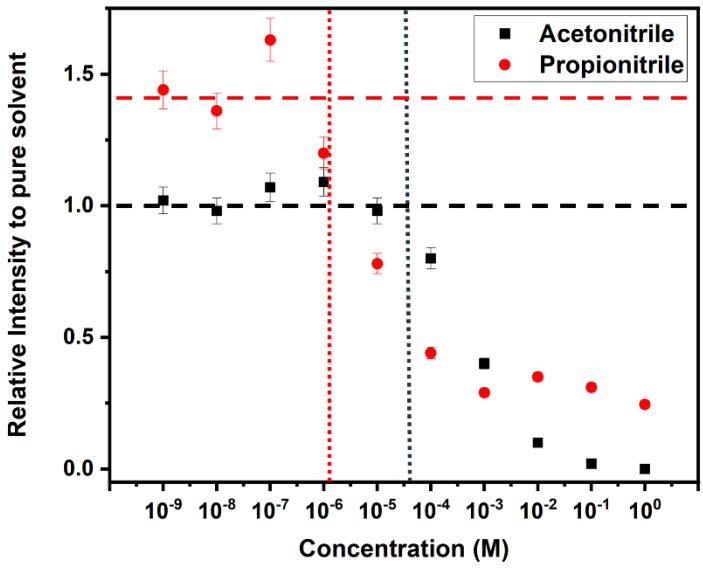

Figure 3.3. VSFG peak intensities of $LiCLO_4$ in acetonitrile and propionitrile relative to the peak intensity of their respective neat samples. The horizontal dashed line indicates the peak intensity of neat solvent. The vertical dashed line indicates the relative concentration region where intensity starts to drop.

As discussed in our previously published work, the increase in intensity compared to the neat liquid is due to the exterior of the second sublayer consisting primarily of cyano groups that point into the bulk liquid.

Consequently, there is an effective negative charge on the outer part of the bilayer. At concentrations of $\sim 3\times10^{-6}$ M and less, our data suggests that lithium ions partition to the exterior of the surface bilayer, causing partial neutralization of the negative effective surface potential. Adsorption of Li^+ could creates a higher degree of alignment of molecules, with the cyano groups pointing up. This effect strengthens the signal from the second sublayer.

Once the cation concentration is high enough to neutralize the charge on the outside of the bilayer, the large ClO_4^- anions are able to enter the bilayer and the cations are able to penetrate the bilayer to reach the polar silica and surface. Anions entering the bilayer make the system more spectroscopically homogenous and hence, with a further increase in salt concentration, the VSFG signal begins to fall rapidly. This trend is seen in both MeCN and EtCN.

We attribute the greater intensity increase in EtCN compared to MeCN to the packing of the bilayer in the two solvents. In molecular simulation work performed previously, we have observed[22] that the CN vectors of the cyanide group in the first sublayer is more parallel to the surface in propionitrile than in acetonitrile. The methylene−methyl vector orientations indicate that in the first sublayer, most propionitrile molecules have their methyl groups pointing parallel to the surface normal. The methyl groups in the outer sublayer are closer to the surface than are the methyl groups in the first sublayer, and are roughly perpendicular to the surface normal. These observations suggest that the EtCN bilayer has highly entangled alkyl groups. As a result, when compared to the overall molecular dimensions, the EtCN bilayer is more compact and ordered than the corresponding MeCN bilayer. Accordingly, we believe that upon interaction with cations, there is more oppurtunity for the cyano groups to reorient and in turn the methylene group in the case EtCN as compared to MeCN and hence the larger increase in relative intensity.

Another detail we notice in Fig 3.3 is that the signal starts to fall away at at lower concentration of electrolyte in EtCN compared to that in MeCN. This observation indicates that anions can begin to enter the bilayer at a somewhat lower concentration in EtCN than in MeCN. We hypothesize that the more compact EtCN bilayer can expand in an accordian-like manner to allow ions to enter. We will test this hypothesis with molecular dynamics simulations.

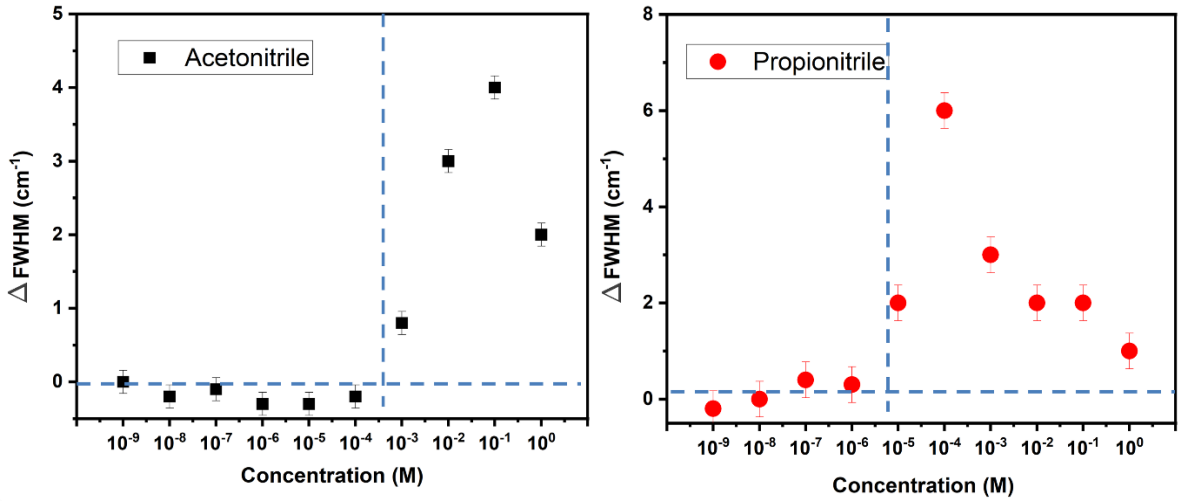

Figure 3.4. FWHM of VSFG spectra of $LiClO_4$ solutions in MeCN and EtCN. The horizontal dashed lines indicate the FWHMs of the neat solvents. The vertical dashed lines indicate the approximate concentration at which the FWHM begins to deviate appreciably from the neat liquid.

Figure 3.4 shows the full width at half maximum (FWHM) of the VSFG spectra for $LiClO_4$ in MeCN and EtCN. The FWHM is roughly constant in MeCN until the salt concentration reaches 1 mM. The FWHM begins to inrease sharply at ~10^{-3} M. However, in the case of EtCN the broadening starts at a concentration of around 10^{-5} M. To understand this behavior we must first consider why the broadening occurs. Once the cations neutralize the effective negative charge on the outer sublayer of the bilayer, the anions no longer face electrostatic repulsion and can enter the bilayer and go to their preferred position in the hydrophobic core. This

partitioning of anions causes a change in electrostatic environment of the methylene groups in the case of EtCN and the methyl groups in the case of MeCN. At low concentrations of anions in the bilayer, some alkyl groups are near anions and others are not, so there is inhomogenous broadening. The FWHM also starts to go down as we keep increasing the concentration of ions. This is because as the concentration of anions in the bilayer increases the electrostatic region around the probed frequencis becomes increasingly homogenous and leads to decrease in FWHM. That the broadening occurring at a lower concentration in EtCN corroborates the conclusions we draw from the intensity data that ions can enter the bilayer at a lower concentration in EtCN than in MeCN.

A similar trend is observed in the red shift of the EtCN VSFG spectra compared to those for MeCN (Figure 3.5). The red-shift begins at the concentration at which the anions are able to penetrate the bilayer. The red shift becomes apparent more than an order of magnitude lower concentrartion of salt in EtCN compared to MeCN. The magnitude of the shift is also larger in magnitude in EtCN (~7 cm^{-1}) than in MeCN (~4cm^{-1}) at a 1 M concentration of $LiClO_4$.

This would be due to the fact that since the EtCN bilayer can expand more, it has more capacity for anions at the same concentration of salt, leading to increased electrostatic environment changes around the methylene bonds. This would lead to a higher shift at the same concentration.

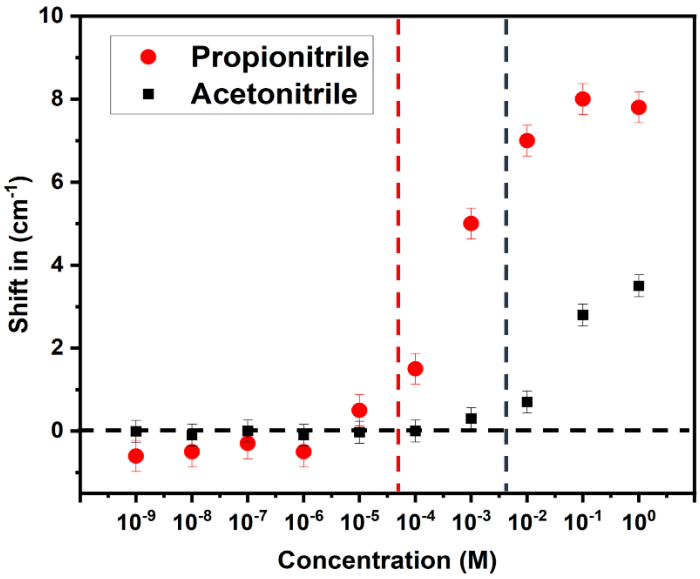

Figure 3.5. The spectral shift relative to the neat solvent. The vertical dashed lines indicate the approximate concentrations at which the red shift becomes apparent.

3.4 Conclusion

The experiments presented here emphasize the importance of solvent organization in determining the ionic distribution, in the liquid–solid system studied here. The comparison between MeCN and EtCN points toward the need for understanding the interfacial organization of ions in electrolyte solutions in polar, aprotic solvents. The VSFG data for $LiClO_4$ in EtCN show trends similar to those observed in MeCN for relative intensity, FWHM, and peak shift. This result offers clues into how the organization of EtCN affects ion interactions with the silica surface. The results indicate that the ions can enter the bilayer at roughly an order of magnitude lower concentration than in MeCN. We hypothesize that this difference is the result of the greater compactnesss of the EtCN bilayer, which allows the bilayer to expand in an accordion-like manner. Our results have important implications for lithium-ion batteries and other electrochemical devices.

3.5 References

(1) Schoch, R. B.; Han, J.; Renaud, P. Transport Phenomena in Nanofluidics. *Rev. Mod. Phys.* **2008**, *80* (3), 839–883.

(2) Vlassiouk, I.; Smirnov, S.; Siwy, Z. Ionic Selectivity of Single Nanochannels. *Nano Lett.* **2008**, *8* (7), 1978–1985. =

(3) Whitehs, B. A. Ion Current Rectification at Nanopores in Glass Membranes. *Langmuir* **2008**, *24* (5), 2212–2218.

(4) Cervera, J.; Schiedt, B.; Ramírez, P. A Poisson/Nernst-Planck Model for Ionic Transport through Synthetic Conical Nanopores. *EPL* **2005**, *71* (1), 35–41.

(5) Siwy, Z. S.; Howorka, S. Engineered Voltage-Responsive Nanopores. *Chem. Soc. Rev.* **2010**, *39* (3), 1115–1132.

(6) Baker, R. W. *Membrane Technology and Applications*; John Wiley& Sons, Inc, 2012.

(7) Mehta, A.; Zydney, A. L. Permeability and Selectivity Analysis for Ultrafiltration Membranes. *J. Memb. Sci.* **2005**, *249* (1–2), 245–249.

(8) Poonam; Sharma, K.; Arora, A.; Tripathi, S. K. Review of Supercapacitors: Materials and Devices. *J. Energy Storage* **2019**, *21*, 801–825.

(9) Bu, F.; Zhou, W.; Xu, Y.; Du, Y.; Guan, C.; Huang, W. Recent Developments of Advanced Micro-Supercapacitors: Design, Fabrication and Applications. *Npj Flex. Electron.* **2020**, *4* (1).

(10) Munje, R. D.; Muthukumar, S.; Panneer Selvam, A.; Prasad, S. Flexible Nanoporous Tunable Electrical Double Layer Biosensors for Sweat Diagnostics. *Sci. Rep.* **2015**, *5* (1), 14586.

(11) Smeets, R.; Keyser, U. F.; Krapf, D.; Wum, -Y; Dekker, N. H.; Dekker, C. Salt Dependence of Ion Transport and DNA Translocation through Solidstate Nanopores. *Nano Lett* **2006**, *6* (1), 89–95.

(12) Roberts, D.; Keeling, R.; Tracka, M.; van der Walle, C. F.; Uddin, S.; Warwicker, J.; Curtis, R. The Role of Electrostatics in Protein-Protein Interactions of a Monoclonal Antibody. *Mol. Pharm.* **2014**, *11* (7), 2475–2489.

(13) Zhang, J.; Liu, X. Y. Effect of Protein–Protein Interactions on Protein Aggregation Kinetics. *J. Chem. Phys.* **2003**, *119* (20), 10972–10976.

(14) Macdonald, R. C.; Bangham, A. D. Comparison of Double Layer Potentials in Lipid Monolayers and Lipid Bilayer Membranes. *J. Membr. Biol.* **1972**, *7* (1), 29–53.

(15) Israelachvili, J. N. Electrostatic Forces between Surfaces in Liquids. In *Intermolecular and Surface Forces*; Elsevier, 2011; pp 291–340.

(16) Honig, B.; Nicholls, A. Classical Electrostatics in Biology and Chemistry. *Science* **1995**, *268* (5214), 1144–1149.

(17) Fenter, P.; Lee, S. S. Hydration Layer Structure at Solid–Water Interfaces. *MRS Bull.* **2014**, *39* (12), 1056–1061.

(18) Joseph, S.; Aluru, N. R. Hierarchical Multiscale Simulation of Electrokinetic Transport in Silica Nanochannels at the Point of Zero Charge. *Langmuir* **2006**, *22* (21), 9041–9051.

(19) Trasatti, S. Relative and Absolute Electrochemical Quantities. Components of the Potential Difference across the Electrode/Solution Interface. *J. Chem. Soc.* **1974**, *70* (0), 1752.

(20) Habib, M. A. Solvent Dipoles at the Electrode-Solution Interface. In *Modern Aspects of Electrochemistry*; Springer US: Boston, MA, 1977; pp 131–182.

(21) Berne, B. J.; Fourkas, J. T.; Walker, R. A.; Weeks, J. D. Nitriles at Silica Interfaces Resemble Supported Lipid Bilayers. *Acc. Chem. Res.* **2016**, *49* (9), 1605–1613.

(22) Ding, F.; Hu, Z.; Zhong, Q.; Manfred, K.; Gattass, R. R.; Brindza, M. R.; Fourkas, J. T.; Walker, R. A.; Weeks, J. D. Interfacial Organization of Acetonitrile: Simulation and Experiment. *J. Phys. Chem. C Nanomater. Interfaces* **2010**, *114* (41), 17651–17659.

(23) Morales, C. M.; Thompson, W. H. Simulations of Infrared Spectra of Nanoconfined Liquids: Acetonitrile Confined in Nanoscale, Hydrophilic Silica Pores. *J. Phys. Chem. A* **2009**, *113* (10), 1922–1933.

(24) Cheng, L.; Morrone, J. A.; Berne, B. J. Structure and Dynamics of Acetonitrile Confined in a Silica Nanopore. *J. Phys. Chem. C Nanomater. Interfaces* **2012**, *116* (17), 9582–9593.

(25) Steiner, P. A. Precision Measurement of Dipole Moments and Other Spectral Constants of Normal and Deuteratedmethyl Fluoride and Methyl Cyanide. *JMol Spectrosc* **1966**, *21* (3), 291–301.

(26) Polster, J. W.; Souna, A. J.; Motevaselian, M. H.; Lucas, R. A.; Tran, J. D.; Siwy, Z. S.; Aluru, N. R.; Fourkas, J. T. The Electrical-double Layer Revisited. *Nat. Sci. (Weinh.)* **2022**, *2* (2).

(27) Souna, A. J.; Motevaselian, M. H.; Polster, J. W.; Tran, J. D.; Siwy, Z. S.; Aluru, N. R.; Fourkas, J. T. Beyond the Electrical Double Layer Model: Ion-Dependent Effects in Nanoscale Solvent Organization. *Phys. Chem. Chem. Phys.* **2024**, *26* (8), 6726–6735.

Chapter 4: Studying polar aprotic solvent mixtures to understand molecular organization at solid–liquid interfaces.

VSFG spectroscopy research conducted by: Siddharth Singh
MD Simulations conducted by: Shahriar Keshvari

4.1 Introduction

So far this dissertation has discussed how solid-liquid interactions can lead to solvent organization at an interface, and how that organization can affect the ion distribution near the surface. I discussed in Chapter 3 how structural differences between solvents, such as those between EtCN and MeCN, can lead to different organizations of the solvent molecules, and thus to different ion distributions. I now consider how mixing two such solvents affects their organization at a silica interface. This question is relevant because solvent mixtures are often used in lithium-ion batteries and other electrochemical devices. There has been an enormous increase in the number of studies electrolytes for lithium-ion batteries recently, because, even with the improvement and developments in safety of the lithium-ion batteries, [1-5] there are still safety problems. Examples of these issues include ignition or gas buildup due to the low thermal stability, the high vapor pressure, and the low flash point of these electrolytes. There is therefore an ever present need to improve the efficiency, stability, and safety of these electrolytes. Most industrial electrolytes are mixtures of ethylene carbonate (EC), diethyl carbonate (DEC) and dimethyl carbonate (DMC), with lithium hexafluorophosphate ($LiPF_6$) as the salt. This type of electrolyte enables a great number of charge–discharge cycles to occur without noticeable loss in capacity. [6-9] We use EtCN–MeCN-d_3 mixture as a model to study these electrolyte-mixture systems. As is the case for EC, DEC, and DMC, EtCN and MeCN-d_3 are polar aprotic solvents with high dipole moments, but the spectroscopy of these nitriles is less complicated. We use MeCN-d_3 so that there is no peak from

the symmetric methyl stretch of MeCN complicating our spectra. We have published work previously on MeCN-MeCN-d_3 mixtures, and will make comparisons with some of those results to understand the EtCN-MeCN-d_3 system better.[10] In that previous work, the methyl symmetric stretch of MeCN at a silica interface was probed for a series of mixtures with MeCN-d_3. The methyl symmetric stretch exhibited a blue shift and a narrowing with isotopic dilution, and the intensity of the spectrum was higher than predicted statistically, particularly at low MeCN concentrations. Molecular dynamics simulations showed that these spectral changes are consistent with the presence of resonant intermolecular vibrational coupling[10], although the dominant mechanism for the frequency shift appears to be repulsive interactions. In this chapter I show that the spectral narrowing also occurs in EtCN upon dilution in MeCN-d_3, but that a blue shift does not. The symmetric methyl stretch of EtCN, which does not appear in VSFG spectra of the neat liquid or salt solutions (Chapter 3), becomes apparent upon dilution with MeCN-d3, offering important insights into the interfacial organization of the mixture. In particular I find that each solvent partitions preferentially into a different sublayer of the surface bilayer.

4.2 Methods

The details of our counterpropagating VSFG spectrometer were given in Chapter 2. For the studies reported here, the probe bandwidth was narrowed to ~5 cm^{-1} (0.3 nm). The probe spectrum used for the experiments reported here was centered at 800 nm. For this study we used only the *SSP* polarization configuration. At the sample, the probe pulse energy was ~15 μJ, and the IR pulse energy was ~14 μJ. The sample consisted of 99+% spectroscopic grade MeCN-d_3 and EtCN, both purchased from SigmaAldrich. The samples were held in an IR-grade quartz cell with a 1-mm path length (FireflySci). The cell was rinsed, oven-dried, and oxygen-plasma cleaned immediately prior to use.

4.3 Results and Discussion

VSFG spectra were first obtained for neat EtCN, after which we proceeded to add MeCN-d_3. Six different solutions were prepared with varying molefraction of MeCN-d_3, as represented by χ_{CD_3CN}. The VSFG spectra of these are shown in Figure 4.1.

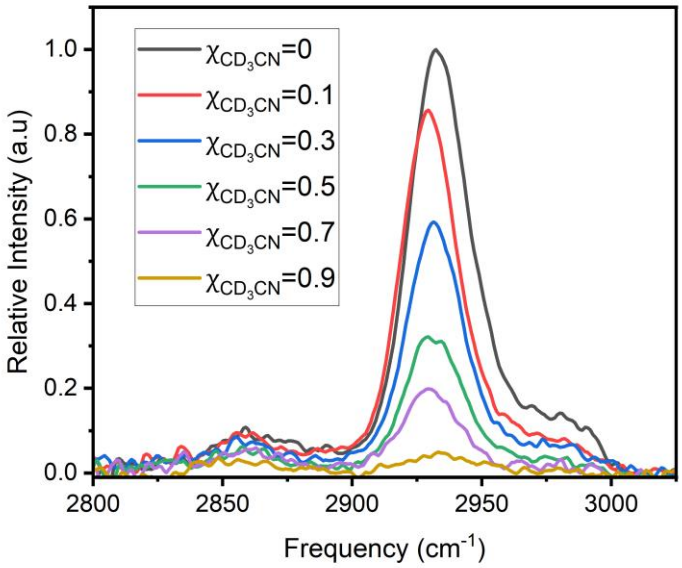

Figure 4.1. VSFG spectra of mixtures of EtCN and MeCN-d_3 at different mole fractions at the silica interface.

As expected, there is a clear decrease in the VSFG intensity with an increasing mole fraction of MeCN-d_3. In our previous work on mixtures of MeCN and MeCN-d_3 at the silica interface, we found that upon isotopic dilution the VSFG intensity of the symmetric methyl stretch at the acetonitrile–silica interface becomes larger than predicted by a simple statistical model in which the Intensity is proportional to the square of the mole fraction of MeCN. Although the observed excess in intensity was modest, there was a clear trend in which the ratio of the observed intensity to the expected intensity grew with increasing MeCN-d_3 mole fraction. This phenomenon was attributed to the fact that with increasing dilution the resonant coupling of the symmetric methyl

stretch of MeCN decreases. The attendant decrease in inhomogenous broadening leads to a narrowing of the spectral contributions of each each sublayer, causing an increase in the signal intensity.[11]

In analogy with these results for the MeCN–MeCN-d_3 system, with increasing mole fraction of MeCN-d_3 in EtCN at the silica interface, the VSFG intensity becomes larger than the statistical prediction (Figure 4.2).

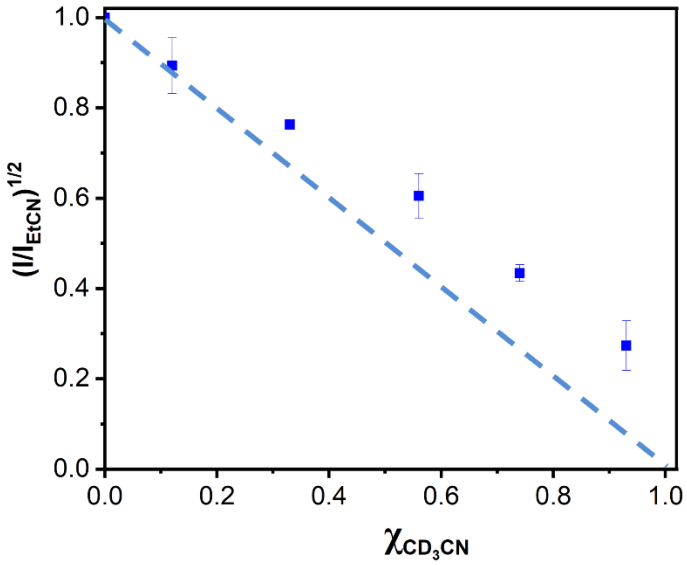

Figure 4.2. The square root of the intensity, relative to that of the neat liquid, of the symmetric methyl stretch peak in the SSP VSFG spectrum of liquid EtCN at the silica interface as a function of the mole fraction of MeCN-d_3. The dashed line is the result expected when the interfacial concentrations mirror those in the bulk and no collective spectroscopic effects are considered.

The deviation from the statistical behavior is roughly an order of magnitude larger than that observed in the MeCN–MeCN-d_3 system. There may be some differences in resonant coupling in the methyl group of MeCN versus the methylene groups in EtCN that contribute to the larger than expected signal in the EtCN–MeCN-d_3 system at high mole fractions of the latter component. As we shall see below, the major contributor to the excess intensity in the EtCN–MeCN-d_3 system is the selective partitioning of the two solvents.

Another interesting feature of the VSFG spectra is a small peak that starts to appear, at ~2870 cm^{-1}, as the mole fraction of MeCN-d_3 increases (Figure 4.3). This spectral region is where the symmetric CH_3 stretch of EtCN should appear. This peak is quite weak in the VSFG spectrum of pure EtCN at the silica interface, presumably due to the roughly centrosymmetric organization. The distance of the methyl group from the cyano group, prevents the inductive effects that lead to different methyl symmetric stretch transition frequencies in MeCN. In EtCN, these effects are instead at play for the methylene group, which is adjacent to the cyano group.

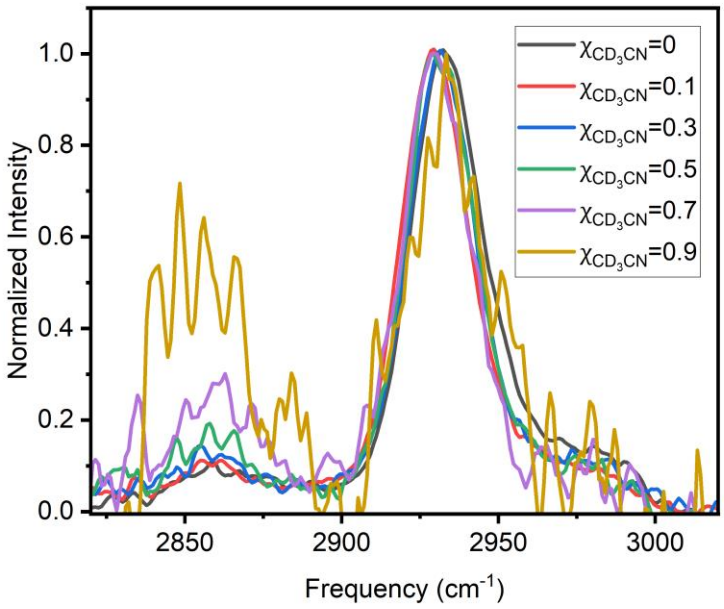

Figure 4.3. Normalized spectra of EtCN–MeCN-d_3 mixtures with varying mole fractions of MeCN-d_3

Why does the peak for the symmetric methyl stretch of EtCN appear in the VSFG spectrum upon dilution with MeCN-d_3? To answer this question, we performed IR spectroscopy experiments on the bulk solutions to ascertain whether this peak arises from a contaminant in the MeCN-d_3. Figure 4.4. shows the IR spectra of these different solutions. There is no peak in the MeCN-d_3 spectra at

2870 cm^{-1}, indicating that the peak in this region of the VSFG spectra indeed arises from EtCN. We therefore theorize that the presence of this spectral feature indicates that MeCN-d_3 partitions preferentially to one of the sublayers of the surface bilayer and EtCN partitions selectively to the other, thereby breaking symmetry. This behavior is consistent with the greater than expected VSFG intensity observed upon dilution for the methylene symmetric stretch peak (Figure 4.2).

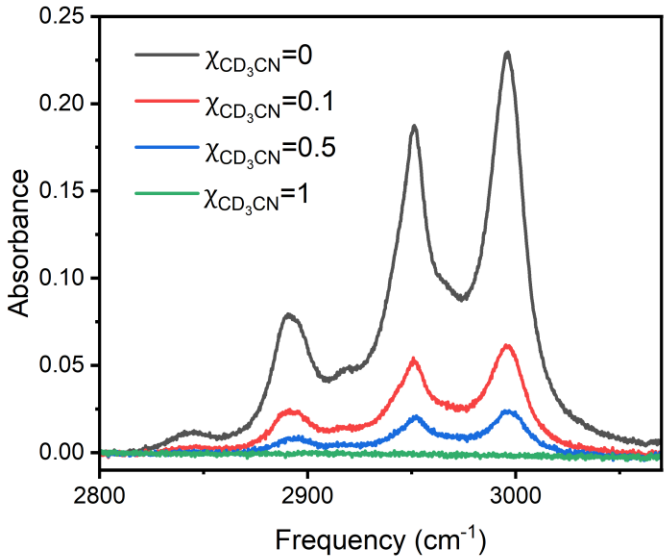

Figure 4.4 IR plots of different mole fraction concentration solution of EtCN–MeCN-d_3

To analyze this behavior further, we performed Gaussian fits to the peaks in the VSFG spectra (Figure 4.5). As shown in figure 4.5A, we first fit each normalized spectrum to a sum of gaussians using MATLAB. We determined the intensity of the symmetric methyl stretch 2870 cm^{-1} from the fits (Figure 4.5B) and calculated the area under this curve. The area under the curve is plotted as a function of the mole fraction of MeCN-d_3 in Figure 4.6.

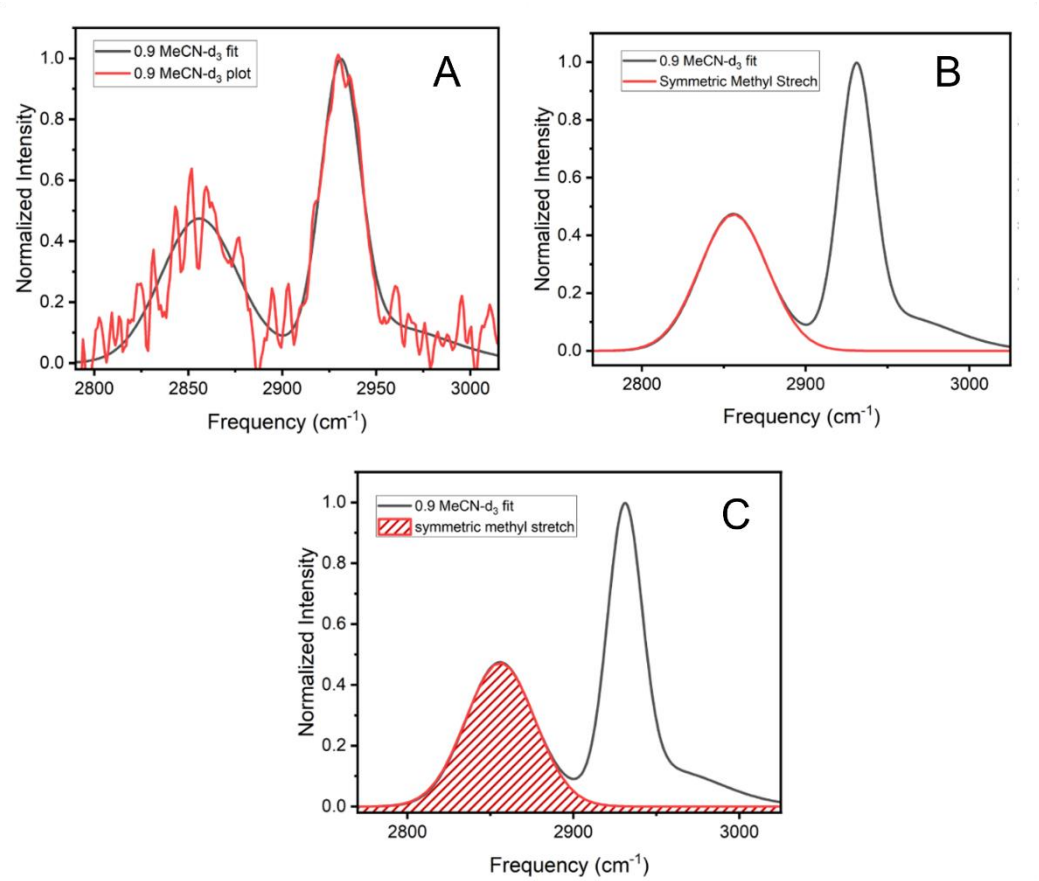

Figure 4.5 Plot showing breakdown of calculation area under curve of symmetric -CH_3 stretching peak. (A) Fit to a single curve of a representative spectrum to multiple gaussian functions. (B) The symmetric methyl stretch contribution in a representative fit. (C) Representative fit, which enables the determination of the area under the curve

The data area-under-the-curve in Fig 4.6 increase with increasing χ_{CD_3CN}. The increase grows rapidly starting at a MeCN-d_3 mole fraction of 0.3, which is similar to the mole fraction at which the deviation from linear behavior starts in Figure 4.2. These data further support the premise that MeCN-d_3 partitions preferentially to one of the two sublayers of the surface bilayer, and EtCN partitions preferentially to the other sublayer.

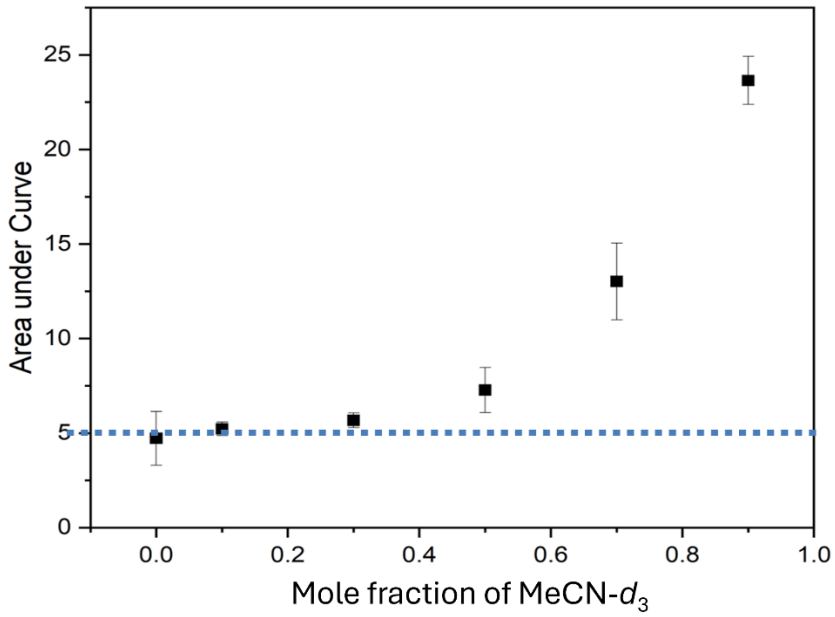

Figure 4.6 Plot of area-under-the-curve for the symmetric methyl stretch peak of EtCN as a function of the mole fraction of MeCN-d_3

My colleague Shahriar Keshvari has performed preliminary simulations of an EtCN–MeCN solvent mixture. These results (Figure 4.7) indicate that EtCN partitions preferentially to the first sublayer of the surface bilayer and is depleted substantially in the second sublayer. This behavior may arise because EtCN loses less entropy when bound to the silica surface than does MeCN. In contrast, MeCN may have more orientational freedom than EtCN in the second sublayer. In Figure 4.7 it is apparent that ρ_{EtCN}/ρ_{MeCN} value is ~1.35 in the first sublayer, and is ~0.6 in the second sublayer. This behavior indicates that EtCN is more than twice as likely to be in the first sublayer as the second.

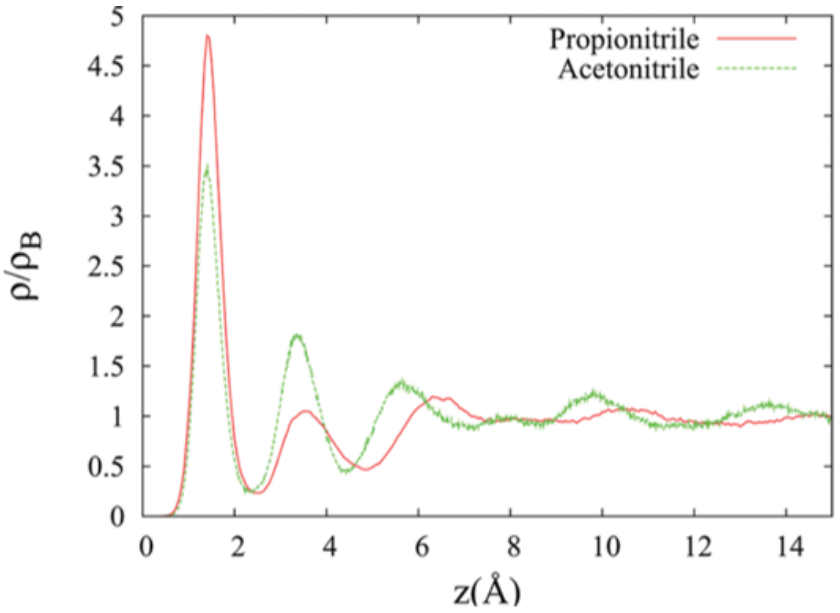

Figure 4.7 Local density of MeCN and EtCN cyano groups, normalized to the bulk density, as a function of distance from the interface. The z coordinate of the plane of the oxygen atoms in the silanol groups is used as the position of the interface, following previous work [12]

4.4 Conclusions and Future Directions

In this chapter I have discussed mixtures of polar aprotic solvents, in an effort to understand how mixing affects the organization of these solvents at the liquid–solid interface. I found that upon an increase in mole fraction of MeCN-d_3 in EtCN, the spectrum of EtCN changes both in intensity and shape. This observation leads us to predict that dilution of the EtCN with a different solvent affects the organization of the surface bilayer in a non-statistical manner with each solvent partitioning selectively to a different sublayer of the surface bilayer.

A weak peak grows in the VSFG spectra at 2870 cm^{-1} upon dilution with MeCN-d_3. This behavior is a clear sign of the preferential partitioning of MeCN-d_3 to one of the sublayers of the bilayer as was confirmed by molecular dynamics simulations. We plan to investigate this behavior further by adding salts to this solvent–mixture system. The change in the VSFG spectra upon the addition of ions will confirm which liquid partitions selectively to the second sublayer of the surface bilayer.

4.5 References

(1) Ozawa, K. Lithium-Ion Rechargeable Batteries with $LiCoO_2$ and Carbon Electrodes: The LiCoO2/C System. *Solid State Ion.* **1994**, *69* (3–4), 212–221.

(2) Botte, G. G.; White, R. E.; Zhang, Z. Thermal Stability of $LiPF_6$–EC:EMC Electrolyte for Lithium Ion Batteries. *J. Power Sources* **2001**, *97–98*, 570–575.

(3) Zhang, Z.; Fouchard, D.; Rea, J. R. Differential Scanning Calorimetry Material Studies: Implications for the Safety of Lithium-Ion Cells. *J. Power Sources* **1998**, *70* (1), 16–20.

(4) Dahn, J.; Fuller, E.; Obrovac, M.; Vonsacken, U. Thermal Stability of Li_xCoO_2, Li_xNiO_2 and λ-MnO_2 and Consequences for the Safety of Li-Ion Cells. *Solid State Ion.* **1994**, *69* (3–4), 265–270.

(5) Vonsacken, U.; Nodwell, E.; Sundler, A.; Dahn, J. Comparative Thermal Stability of Carbon Intercalation Anodes and Lithium Metal Anodes for Rechargeable Lithium Batteries. *Solid State Ion.* **1994**, *69* (3–4), 284–290.

(6) Xing, L.; Li, W.; Wang, C.; Gu, F.; Xu, M.; Tan, C.; Yi, J. Theoretical Investigations on Oxidative Stability of Solvents and Oxidative Decomposition Mechanism of Ethylene Carbonate for Lithium Ion Battery Use. *J. Phys. Chem. B* **2009**, *113* (52), 16596–16602.

(7) Xing, L.; Zheng, X.; Schroeder, M.; Alvarado, J.; von Wald Cresce, A.; Xu, K.; Li, Q.; Li, W. Deciphering the Ethylene Carbonate-Propylene Carbonate Mystery in Li-Ion Batteries. *Acc. Chem. Res.* **2018**, *51* (2), 282–289.

(8) Kimura, K.; Tominaga, Y. Understanding Electrochemical Stability and Lithium Ion-dominant Transport in Concentrated Poly(Ethylene Carbonate) Electrolyte. *ChemElectroChem* **2018**, *5* (24), 4008–4014.

(9) Metzger, M.; Walke, P.; Solchenbach, S.; Salitra, G.; Aurbach, D.; Gasteiger, H. A. Evaluating the High-Voltage Stability of Conductive Carbon and Ethylene Carbonate with Various Lithium Salts. *J. Electrochem. Soc.* **2020**, *167* (16), 160522.

(10) Souna, A. J.; Cohen, S. R.; Rivera, C. A.; Manfred, K.; Coasne, B.; Fourkas., J. T. The Role of Resonant Coupling in Vibrational Sum-Frequency-Generation Spectroscopy: Liquid Acetonitrile at the Silica Interface. *J. Mol. Liq.* **2023**, *375* (121315), 121315.

(11) Loughnane, B. J.; Scodinu, A.; Farrer, R. A.; Fourkas, J. T.; Mohanty, U. Exponential Intermolecular Dynamics in Optical Kerr Effect Spectroscopy of Small-Molecule Liquids. *J. Chem. Phys.* **1999**, *111* (6), 2686–2694.

(12) Z. Hu, J.D. Weeks, Acetonitrile on Silica Surfaces and at Its Liquid-Vapor Interface: Structural Correlations and Collective Dynamics, *J. Phys. Chem. C* **2010,** 114, 10202

Chapter 5: Gating Ion and Fluid Transport with Chiral Solvent

Adapted from: Silva, S.; Singh, S.; Cao, E.; Fourkas, J. T.; Siwy, Z. S. *Faraday Discuss.* **2023**, *246* (0), 508–519.
VSFG spectroscopy research conducted by: Siddharth Singh
Ion transport research designed and conducted by: Savannah Silva and Ethan Cao

5.1 Introduction

Chirality plays a fundamental role in life. There have been significant efforts made to develop technologies to separate racemic mixtures to create enantiomerically pure samples[1-3] and to perform asymmetric synthesis[4] to provide enantiomerically pure product. Biological channels[5-7] and artificial nanopores[8, 9] have been used to create systems that can distinguish between enantiomeric analytes and to prepare filtration systems capable of transporting a single enantiomer with high selectivity.[10-12] Chiral solvents can also facilitate asymmetric catalysis in some cases.[13] In this manuscript we consider racemic and enantiomeric propylene carbonate (PC), and ask whether the chiral character of the solvent can affect its organization at solid/liquid interfaces. We probe the influence of the solvent chirality on the effective surface potential of a silica/liquid interface over a range of $LiClO_4$ concentrations. PC is an especially interesting solvent, because being aprotic it is not expected to induce deprotonation of the silanol groups on silica. Yet PC molecules feature a dipole moment of 4.9 D, and the racemic form of this solvent has been shown to induce an effective positive potential of the solid/liquid interface in polymer and glass nanopores.[14, 15] The origin of the positive potential was hypothesized to stem from possible adsorption of lithium ions, as well as from organization of the solvent molecules at the interface.[16] If the solvent organization is indeed responsible for the finite effective potential of silica in PC, then the interfacial molecular arrangement and effective potential are expected to be sensitive to whether the solvent is racemic or enantiomerically pure. Consequently, porous media would be

expected to exhibit different ionic and fluidic transport for the same concentration of electrolyte but different forms of the solvent. Note that the interfacial arrangement of the solvent could determine the effective surface potential through local charges of the dipole molecules, as well as affecting location of ions within and outside of the layers.[16]

To probe the interfacial organization of PC, as well as presence and polarity of the effective surface potential on silica, we combined two experimental approaches. First, we used vibrational sum-frequency-generation spectroscopy (VSFG)[17, 18] to determine the molecular organization of racemic and enantiomerically pure PC at the silica/liquid interface. Next, electrokinetic experiments were performed to determine the effective potential of the interface. [19] To this end, electroosmosis was measured as a function of $LiClO_4$ concentration in polymer and silicon nitride pores. We note that a similar approach has been recently applied to probe solid/liquid interface of silica and acetonitrile-based electrolyte solutions.[16] Acetonitrile is also characterized by a high dipole moment, 3.9 D, and was found to create a highly organized, lipid-bilayer-like (LBL) structure in which the cyano groups accept hydrogen bonds from the silica silanol groups.[19] The spatial organization of acetonitrile was preserved even in 1 M $LiClO_4$, and governed the locations of the cations and anions at all concentrations studied.[16] In this manuscript we show that PC also creates a spatially organized structure on the silica interface that is sensitive to chirality of the solvent. Electroosmosis measured in salt gradients allows us to conclude that it is the solvent organization that primarily influences ionic and fluidic transport, in contrast to the predictions of EDL theory.

5.2 Materials and Methods

5.2.1Chemicals

Lithium perchlorate ($LiClO_4$, ≥99.99% battery grade, Sigma Aldrich), racemic propylene carbonate (Sigma Aldrich with 99.7% pure HPLC Grade), R and S enantiomers of propylene carbonate (TCI chemicals, purity >98%) were used in the experiments. Propylene carbonate was stored in glovebox, and small amounts of the solvents were taken out to prepare solutions that were used within few hours.

5.2.2 VSFG experiments

VSFG experiments were performed as described previously.[20] Briefly, in the VSFG spectrometer setup, a Ti:sapphire oscillator (Mira Basic, Coherent) is used to seed a regenerative amplifier (Legend Elite, Coherent). The amplifier generates pulses of 800 nm with pulse duration of 80 fs and repetition rate of 1 kHz. The amplifier output has an average power of 3 W, 1 W of which is directed into an OPA/DFG module (TOPAS, Light Conversion) to produce an IR beam centered at 2945 cm^{-1} with a bandwidth of 250 cm^{-1} and a maximum pulse energy of 15 μJ. This IR beam helps probe vibrations in the C–H stretching region of the infrared spectrum. The remaining power of the amplifier output is sent through a delay stage via a slit in a 4f pulse stretcher to the sample. The slit is used to narrow the bandwidth to 5 cm^{-1}. This probe beam is 15 μJ of 800 nm light. The IR and probe beams thus generated are made to meet at the sample in a counter-propagating geometry. The probe and infrared beams are incident at 61° and −58° from the surface normal, respectively. The signal is generated at a −32.8° angle and is collected using a spectrometer (ActonSP300i) with a thermoelectrically cooled CCD camera (Spec-10:100, Roper Scientific). The experiments were performed in the SSP, PPP and SPS with the polarizations listed in the order of the signal, probe, and IR beams. P denotes polarization parallel to the surface normal and S

denotes polarization perpendicular to the surface normal. Eight 120 s long scans were performed for each sample.

The individual spectra were normalized to the nonresonant SFG signal of a gold substrate. A polystyrene film placed in the path of the IR beam while measuring the gold SFG signal was used to frequency calibrate the signal using four absorption peaks of the polystyrene. The cleaning process before usage for the cuvettes involved rinsing with contaminant-free acetone, methanol, and then water. The cuvettes were then oven-dried, and cleaned for 3 min in an oxygen plasma.

5.2.3Pore preparation

Two types of pores were used in measurements: single nanopores in or 20 nm thick silicon nitride and single pores in 12-□m-thick polyethylene terephthalate (PET). Silicon nitride pores were purchased from Norcada and had an opening diameter of 30 nm.

Single polymer pores in PET were prepared using the track-etching technique, which entails irradiation with a single, energetic heavy ion (UNILAC at the Institute for Heavy Ions Research in Darmstadt, Germany) and subsequent etching in 2 M NaOH at 50 °C.[21, 22] These etching conditions have been shown previously to lead to the formation of symmetric pores. The diameters of these single pores were estimated by assuming that the pores were filled with bulk solution and that the pore shape was cylindrical. Sizing of all pores was performed in an aqueous solution of 1 M KCl. Experiments with pores of diameters 370 nm and 450 nm are presented in this manuscript. The PET films had a circular shape with a 3 cm diameter, and the single pore was located within a 100 □m circle in the middle that was the location of the opening of a metal mask that restricted access of the heavy ions to this region. This relatively small area exposed to the heavy ions in a

defocused beam enabled one to restrict the number of ions passing through to one.[23] Consequently, all membranes used in this study contained only one pore.

5.2.4 Ion-current measurements

Electrokinetic characterization of single pores was performed in a home-made conductivity cell where a single pore membrane separated two chambers of a conductivity cell. Two different designs of conductivity cell were used to accommodate a larger size of a PET film and a much smaller TEM chip. Each membrane was exposed to a concentration gradient of $LiClO_4$ prepared either in racemic or enantiomeric PC. The concentration gradients used were 0.1 mm/1 mM, 0.5 mM/5 mM, 1 mM/10 mM, and 10 mM/100 mM. Current–voltage curves were recorded using Keithley 6487 picoammeter/voltage source (Keithley Instruments, Cleveland, OH) and two pellet Ag/AgCl electrodes. The voltage was changed between -2 V and +2 V with 0.1 V steps. Before switching salt concentration, both chambers of the conductivity cell were soaked thoroughly in PC.

5.3 Results and Discussion

5.3.1 VSFG spectra of racemic and enantiomeric propylene carbonate

To probe whether PC forms a spatially organized structure on the silica surface, VSFG measurements were performed on a flat IR quartz substrate in contact with racemic or enantiomerically pure PC (Figure 1). VSFG is uniquely sensitive to the arrangement of molecules at interfaces between isotropic media, where symmetry is broken, because within the electric dipole approximation the VSFG signal of an isotropic or centrosymmetric medium is zero.[24] The polarization configuration that we measure is described in terms of the signal polarization, the 800-nm probe polarization, and the tunable IR pump polarization. Each polarization combination has

a different sensitivity to the orientations of the IR transition dipoles, and hence can give us information on the orientation of the molecules at the interface. The SSP polarization configuration is most sensitive to IR transition dipoles that have a significant projection along the surface normal, the SPS polarization configuration is most sensitive to IR transition dipoles that have a significant projection along the surface, and the PPP polarization configuration is sensitive IR transition dipoles with a significant projection in either of these directions.

Figure 2A shows VSFG signals in all three polarization configurations in the C-H stretching region for racemic PC. PC has a methyl group, and methylene group, and a methine group. The former two groups have both symmetric and asymmetric stretches. All of the C-H stretching modes are both IR and Raman active, and so should show up in the VSFG spectrum. The modes for individual groups cannot be distinguished in these spectra. The likely causes for the broad peaks include spectral overlap, the existence of two nearly isoenergetic conformers (with the methyl group axial and equatorial), possible mode mixing, and the potential presence of Fermi resonances. The two broad peaks that we observe can generally be attributed, however, to symmetric C-H stretches (~2920 cm^{-1}) and asymmetric C-H stretches (~2980 cm^{-1}) The SSP signal is considerably stronger than the SPS or PPP signals, which we attribute to unfavorable nonlinear Fresnel factors for the latter two polarization configurations. In all cases the peak for the asymmetric stretches is stronger than that for the symmetric stretches. The prominence of the asymmetric stretches in the SSP spectrum suggests that the methyl and methylene groups have a substantial projection along the surface. The fact that the symmetric stretch signal is somewhat stronger in relation to the asymmetric stretch signal in the other polarization configurations supports this picture. The symmetric stretch peak likely remains weaker than the asymmetric stretch peak under SPS and

PPP conditions because symmetric C-H stretches are generally strongly polarized, whereas asymmetric stretches are depolarized.

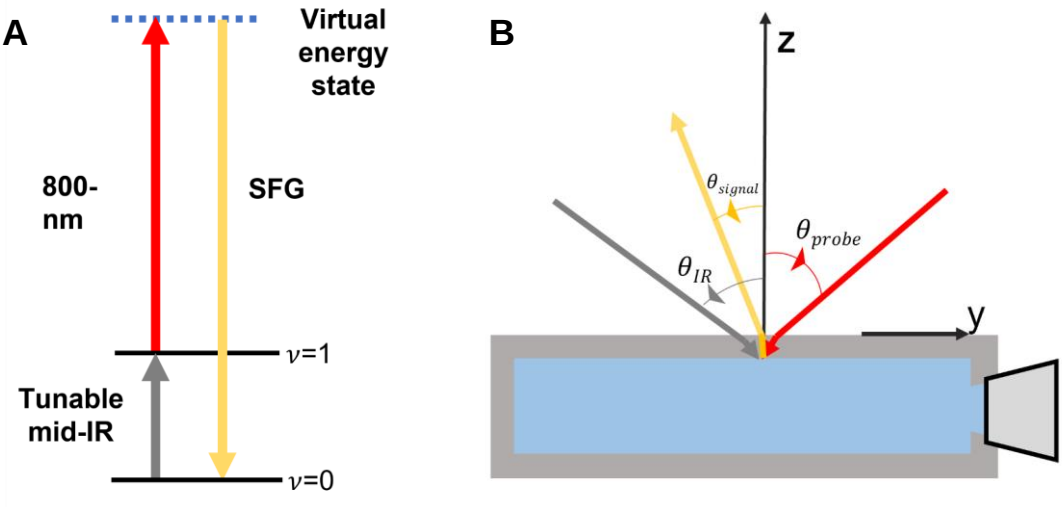

Figure 5.1. The VSFG spectroscopy scheme used to obtain results presented in this manuscript. (A) A Jablonski diagram of the VSFG process. An IR pump beam excites a vibration that is IR active. The vibration is then probed via a Raman transition through a virtual state, which is driven by an 800-nm laser, generating a signal at the sum of the two frequencies. (B) A schematic of the counter-propagating VSFG spectrometer used to obtain the data in this paper. The IR and probe beams approach an IR quartz cuvette filled with the solvent from opposite directions, yielding a signal that propagates in a unique direction.

Let's first revisit VSFG spectra and molecular structure of acetonitrile at a silica interface. The first sublayer of the acetonitrile LBL structure at the interface is composed largely of molecules that accept hydrogen bonds from surface silanol groups.[19] Due to inductive effects, this hydrogen bonding leads to a shift in the symmetric methyl stretching frequency compared to that of the molecules in the second sublayer, which do not accept hydrogen bonds. This shift causes acetonitrile to have a strong VSFG signal for the symmetric methyl stretch at this interface.

The carbonyl group of PC is also expected to accept hydrogen bonds from surface silanol groups. However, because there are no hydrogen atoms bonded to the carbons that are adjacent to the

carbonyl group, any inductive effects in the C-H stretching frequencies are expected to be minimal. The weak VSFG signal for PC at this interface is therefore suggestive of the formation of a relatively centrosymmetric surface organization, i.e. a LBL structure. As discussed below, electrochemical measurements support this picture.

Figure 2B compares VSFG spectra in the SSP polarization configuration for racemic and enantiomerically pure (R and S) PC. The spectra for the two enantiomers are comparable. However, both peaks are considerably stronger for the enantiomerically pure liquids than for the racemic liquid, although the signal is still considerably smaller than that for acetonitrile at the same interface. Furthermore, the symmetric and asymmetric stretch peaks are of comparable heights for the enantiomerically pure liquids. The stronger VSFG signal for the enantiomerically pure PC suggests that a single enantiomer cannot form an LBL structure that is as well organized as that formed in the racemic liquid, leading to a reduced cancellation of signals from molecules pointing in opposite directions at the interface.

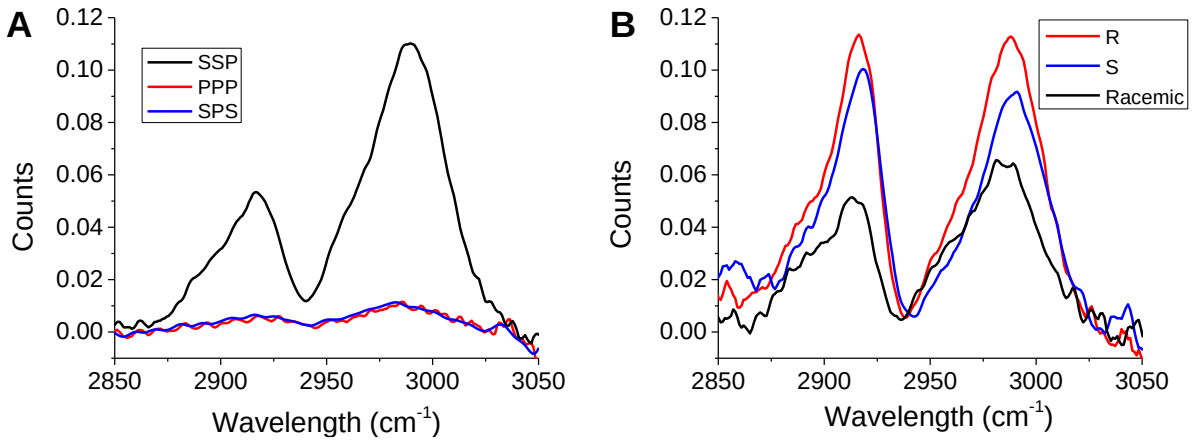

Figure 5.2. (A) VSFG spectra of neat racemic propylene carbonate at silica interface at three configurations of the transitional dipoles. (B) SSP VSFG spectra of racemic and the R and S enantiomers of PC at the silica interface.

However, the VSFG signal is still relatively weak for the enantiomerically pure liquids, suggesting that an LBL structure does still persist. The enhancement of the symmetric stretch signal further suggests that the methyl and methylene groups may have a greater projection along the surface normal in the enantiomerically pure liquid.

5.3.2 Electroosmosis in $LiClO_4$ solutions in enantiomeric and racemic PC.

Our VSFG measurements suggest that enantiomerically pure and racemic samples of PC both exhibit spatial organization at a silica interface. As the next step, we probed the consequences of the interfacial structure for ionic and fluidic flow. Specifically, we sought to determine whether electroosmosis in PC is sensitive enough to detect differences in the interfacial organization of the racemic and enantiomerically pure liquids that were revealed by VSFG.

Figure 3 shows a scheme of our experimental setup in which a single pore is placed in contact with a salt concentration gradient. The presence of different salt concentrations on both sides of the membrane naturally leads to ion-current rectification, but only when the interface exhibits finite potential.[22] If the ground electrode is located in the less concentrated solution and the interface carries an effective negative potential, the direction of electroosmosis will be determined by the cations, which will electroosmotically drag the more concentrated solution into the pore at positive voltages (Figure 3A). When negative voltage is applied, again keeping the ground in the less concentrated solution, a pore with negative potential will be filled with the solution of lower concentration. Consequently, an asymmetric current-voltage curve will be recorded such that $|I(+V)| > |I(-V)|$. If the pore carries effective positive potential, the direction of electroosmosis will be determined by the anions, and the current at negative voltages will be higher in magnitude than at positive voltages (Figure 3B).

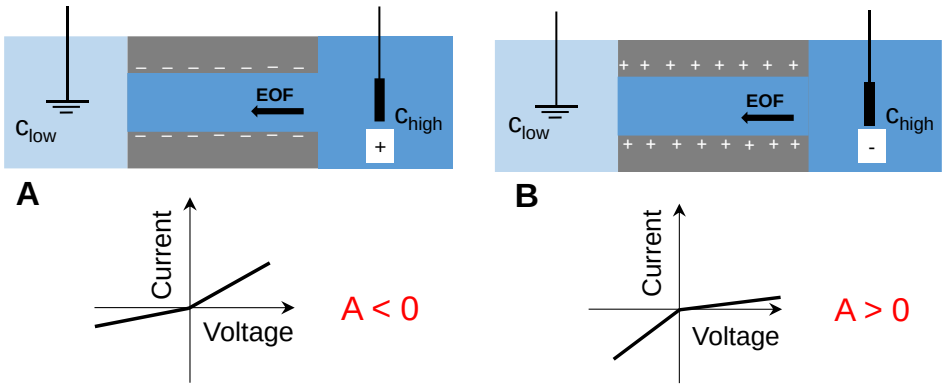

Figure 5.3. Scheme of an experimental set-up where a single pore is in contact with a salt concentration gradient. The ground electrode is placed in the solution with lower salt concentration, c_{low}. (A) A pore with negative effective surface potential will be filled with the more concentrated solution, c_{high}, for positive transmembrane potentials when the direction of electroosmosis is from c_{high} to c_{low}. More ions in the pore will lead to recording higher currents, than for negative voltages, when the pore is filled with the less concentrated solution. (B) A pore with positive surface potentials will be filled with the more concentrated solution for negative voltages, because in this case the direction of electroosmosis is determined by the migration of anions. Consequently, a current-voltage curves will be recorded such that negative currents are larger than positive currents. The parameter A is ion current anisotropy defined in eq. (1).

The level of asymmetry of the current–voltage curves provides an indirect measure of the magnitude of the effective surface potential. For high surface potentials, electroosmosis can fill the entire volume of the pore with a solution of either lower or higher concentration.[22] Consequently, the ratio of currents measured at positive and negative voltages will be equal to the ratio of the ionic conductivities of the solutions. If, on the other hand, the surface potential allows only a part of the pore volume to be filled with solution on either side, the observed asymmetry will be lower. All I-V curves were characterized by ion current anisotropy, *A*, parameter, defined in our previous publication as:[16]

$$A(V) = \frac{I(-V) + I(V)}{I(-V) - I(V)} \qquad \text{eq. (1)}$$

In our electrode configuration, the parameter *A* assumes positive values when a pore has effective positive potential, and negative values when the interface has negative potential. Figure 4 A-C shows example recordings of current-voltage curves and the parameter *A* for a single PET pore with diameter of 450 nm and a single silicon nitride pore with an opening of 30 nm. Recordings were performed with solutions prepared using racemic PC and solutions based on enantiomeric PC (R).

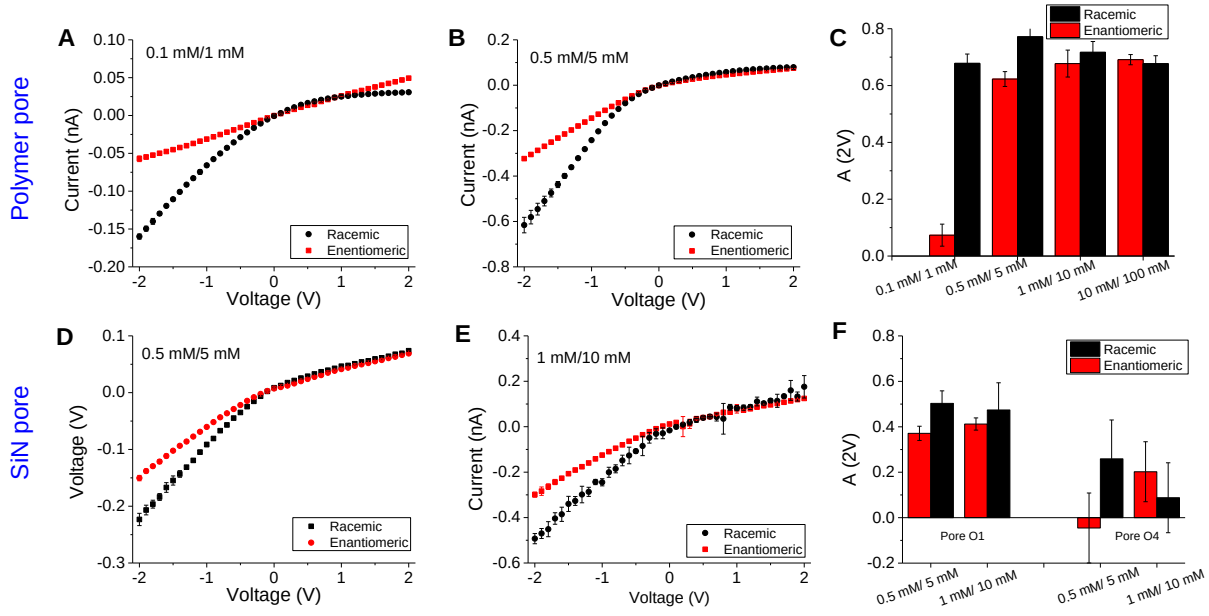

Figure 5.4. Recordings for a single 450 nm in diameter PET pore (A-C) and a single 30 nm in diameter silicon nitride pore (D-F) with current-voltage curves and summary of the anisotropy parameter, A, defined by eq. (1). The bar graph in (F) shows the parameter A for two independent pores, O1 and O4.

When the PET pore was in contact with the lowest concentration gradient of 0.1 mM and 1 mM $LiClO_4$, the recordings in the racemic solutions suggested that this pore exhibited effective positive

potential. Yet, the same pore in the same concentration gradient prepared using the enantiomeric PC exhibited nearly linear current-voltage curve indicating the effective surface potential was close to zero.

As the concentration increased on both sides of the pore by a factor of five, the pore rectified in the same direction in both racemic and enantiomeric PC but the anisotropy parameter was again higher in the racemic case. As the ion concentrations increased further, the I-V curves for both types of solutions became identical. A set of data for an independently prepared pore with an opening of 370 nm is shown in Supporting Information, Figure S1.

The data for the silicon nitride nanopores were more difficult to record due to the challenges of 'wetting' the 30 nm pore with viscous propylene carbonate. We chose pores with this opening diameter due to the small thickness of the silicon nitride films. In order to induce electroosmosis-based rectification in salt concentration gradients, the pore has to have a finite aspect ratio such that the transport properties are still influenced by the ionic concentration in the pore and not at the pore mouth in region of access resistance.[25] Similar to the PET pores, however, recordings in racemic 0.5 mM/ 5 mM solutions indicated the surface potential was positive. The current values at the lowest concentrations of 0.1 mM/1 mM were for some pores unstable and we are not reporting values of *A* for this gradient. Current-voltage curves in enantiomeric solutions, in general, also exhibited less ion current rectification than in racemic PC, similar to the recordings for PET pores. Figure 4 D-F shows recordings for one 30 nm in diameter SiN pore (designated as O1). Values of the parameter *A* for another SiN pore (O4) are also shown in Figure 4F. Due the difficulties with the pore wetting, we report recordings in only two concentration gradients.

The recordings with SiN pores were also challenging, because in some cases the recorded currents in the same concentration gradient of $LiClO_4$ were significantly different in racemic and

enantiomeric solutions for both voltage polarities suggesting that the pores had different resistances (Figure S2). We do not have yet explanation for this effect, because the salt concentration in on all solutions was carefully controlled, and ionic conductivity of chiral and racemic solutions is expected to be the same.[26] Figure 4D-F was, however, created based on recordings where the pore conductances in the linear regime of current-voltage curves were the same at a given concentration gradient in racemic and enantiomeric solutions, as seen in PET pores. Identical conductances in the linear regime gave us confidence that we were capturing nonlinear effects that stem from different effective surface potentials.

The positive effective potential in the presence of $LiClO_4$ solutions in propylene carbonate was observed in multiple samples of SiN and polymer pores. Since all silicon nitride pores were incubated in piranha solution prior to use, the created silanol groups created a surface that was similar in its chemical properties to that of the glass surface used in VSFG experiments. PET surface on the other hand contains carboxyl groups at a very high density of up to 1 per nm^2.[27] We postulate that the effective positive potential of the solid/liquid interface originates from the interfacial organization of the solvent in both silica/liquid and polymer/liquid interfaces that dictates the interfacial ionic distributions.

It is important to note that some pores studied here exhibited effective positive potential already in the gradient with lowest concentrations, 0.1 mM/1 mM. On the other hand, glass pores in contact with 0.1 mM/1 mM $LiClO_4$ solutions in acetonitrile exhibited negative effective potential, which we attributed to the organized layer of the solvent molecules and unscreened partial negative charges on nitrogen.[16] Only in the gradient of 1 mM/10 mM did the glass pores exhibited effective positive surface potential. The observation of positive potential in a wider range of $LiClO_4$

concentrations in propylene carbonate than in acetonitrile points to the possibility for lithium ions to partition into the bilayer at lower concentrations.

Finally, what could be the reason for the lower positive potential in the chiral solutions? We believe a molecular picture of what is happening at the interface can be gleaned from the VSFG spectra. The racemic PC creates a more centrosymmetric system with the solvent molecules being more ordered in the first layer compared to the enantiomeric system. Consequently, the LBL in racemic solutions will impose different partition coefficients for cations and anions to enter the bilayer and will dictate location of both ions in a concentration dependent manner.[16] Lithium will accumulate on the bilayer surface and be more likely to enter the bilayer due to partial negative charges on the oxygen atoms. The interface can then become positively charged at already low $LiClO_4$ concentrations. We expect that with the addition of more concentrated racemic solutions, the solvent organization becomes weaker, similar to what we saw with acetonitrile.

Enantiomeric PC creates a more disordered bilayer such that possibly both cations and anions can enter the bilayer, which would lower the effective positive potential. With the increase of salt concentration, the layers in racemic and enantiometic solvents have similar organization leading to similar values of the anisotropy A parameter.

5.4 Conclusions

Combined VSFG and electrokinetic measurements have revealed that propylene carbonate creates interfacial structure whose details are sensitive to the chirality of the solvent. Racemic propylene carbonate creates a layered structure at the silica interface that is more ordered than the enantiomeric one. Results for both types of PC, are however in strong contrast to the classic picture

of the electrical double-layer where solvent is treated as a homogenous continuum. Our results also point to the possibility of tuning ionic and fluidic transport with solvent chirality. The chirality-controlled transport is a consequence of chirality governed molecular structure of the interface and the effective surface potential.

5.5 References

(1) Y. Okamoto and T. Ikai, *Chem Soc Rev*, 2008, **37**, 2593-2608.

(2) Q. Cheng, Q. Ma, H. Pei and Z. Mo, *Separation and Purification Technology*, 2022, **292**, 121034.

(3) M. Ciriani, R. Oliveira and C. A. M. Afonso, *Green Chemistry*, 2022, **24**, 4328-4362.

(4) E. M. Carreira and L. Kvaerno, *Classics in stereoselective synthesis*, Wiley-VCH, Weinheim ;, 2009.

(5) J. A. Cooper, S. Borsley, P. J. Lusby and S. L. Cockroft, *Chem Sci*, 2017, **8**, 5005-5009.

(6) A. J. Boersma and H. Bayley, *Angewandte Chemie International Edition*, 2012, **51**, 9606-9609.

(7) J. Wang, J. D. Prajapati, F. Gao, Y.-L. Ying, U. Kleinekathöfer, M. Winterhalter and Y.-T. Long, *J Am Chem Soc*, 2022, **144**, 15072-15078.

(8) F. Zhang, Y. Sun, D. Tian and H. Li, *Angewandte Chemie International Edition*, 2017, **56**, 7186-7190.

(9) C. Han, X. Hou, H. Zhang, W. Guo, H. Li and L. Jiang, *J Am Chem Soc*, 2011, **133**, 7644-7647.

(10) Z. Sun, J. Hou, L. Li and Z. Tang, *Coordination Chemistry Reviews*, 2020, **425**, 213481.

(11) B. Lakshmi and C. R. Martin, *Nature*, 1997, **388**, 758-760.

(12) S. B. Lee, D. T. Mitchell, L. Trofin, T. K. Nevanen, H. Söderlund and C. R. Martin, *Science*, 2002, **296**, 2198-2200.

(13) Y. Nagata, R. Takeda and M. Suginome, *ACS Central Science*, 2019, **5**, 1235-1240.

(14) T. Plett, W. Q. Shi, Y. H. Zeng, W. Mann, I. Vlassiouk, L. A. Baker and Z. S. Siwy, *Nanoscale*, 2015, **7**, 19080-19091.

(15) R. A. Lucas, C.-Y. Lin and Z. S. Siwy, *The Journal of Physical Chemistry B*, 2019, **123**, 6123-6131.

(16) J. W. Polster, A. J. Souna, M. H. Motevaselian, R. A. Lucas, J. D. Tran, Z. S. Siwy, N. R. Aluru and J. T. Fourkas, *Natural Sciences*, **n/a**, e20210099.

(17) M. Buck and M. Himmelhaus, *Journal of Vacuum Science & Technology A*, 2001, **19**, 2717-2736.

(18) F. Vidal and A. Tadjeddine, *Reports on Progress in Physics*, 2005, **68**, 1095.

(19) B. J. Berne, J. T. Fourkas, R. A. Walker and J. D. Weeks, *Accounts Chem Res*, 2016, **49**, 1605-1613.

(20) F. Ding, Z. Hu, Q. Zhong, K. Manfred, R. R. Gattass, M. R. Brindza, J. T. Fourkas, R. A. Walker and J. D. Weeks, *The Journal of Physical Chemistry C*, 2010, **114**, 17651-17659.

(21) S. Müller, C. Schötz, O. Picht, W. Sigle, P. Kopold, M. Rauber, I. Alber, R. Neumann and M. E. Toimil-Molares, *Crystal Growth & Design*, 2012, **12**, 615-621.

(22) Y. H. Qiu, R. A. Lucas and Z. S. Siwy, *J Phys Chem Lett*, 2017, **8**, 3846-3852.

(23) R. Spohr, 1983.

(24) P. N. Butcher and D. Cotter, *The Elements of Nonlinear Optics*, Cambridge University Press, 1990.

(25) C. Lee, L. Joly, A. Siria, A.-L. Biance, R. Fulcrand and L. Bocquet, *Nano Lett*, 2012, **12**, 4037-4044.

(26) P. Jankowski, K. Grzegorzewska, A. Szabłowska, M. Piszcz, M. Dranka, G. Z. Żukowska and M. Kalita, *Electrochim Acta*, 2015, **175**, 240-246.

(27) A. Wolf, N. Reber, P. Y. Apel, B. E. Fischer and R. Spohr, *Nuclear Instruments and Methods in Physics Research Section B: Beam Interactions with Materials and Atoms*, 1995, **105**, 291-293.

Chapter 6: Chiral Electrokinetic Phenomena in Single Nanopores

Adapted from: Kristen Alanis,[#] Savannah A. Silva,[#] Siddharth Singh,[#] Kabin Lin, Tilman E. Schäffer, John T. Fourkas,' Lane. A. Baker, Zuzanna S. Siwy (*submitted for publication*)

[#]These Authors contributed equally

VSFG spectroscopy research conducted by: Siddharth Singh and Ovuokenye Omadoko
Ion transport research designed and conducted by: Savannah Silva
Electrokinetic experiments in nanopipettes was conducted by: Kristen Alanis

6.1 Introduction

Solid–liquid interfaces play key roles in biology, sensing, separation and energy storage systems, e.g. batteries, supercapacitors.[2] The interface between a surface and aqueous solution is often described using the continuum model provided by the Poisson-Boltzmann equation[2o, 2p, 3] when considering biological or biosensing systems. In this model, ions are treated as point charges and the solvent is described as a homogeneous continuum. On the other hand, the interface between a surface and a non-aqueous solution – where the classical model of the electrical double layer might not apply[2c, 4] [5] – is of importance in separation processes and energy-storage devices. Electrochemical platforms that rely on lithium salts in carbonate solvents are a preeminent example of the importance of interfaces in non-aqueous electrolyte systems.[6] Here, with the goal of developing a deeper understanding of non-aqueous interfaces, we probe propylene carbonate (PC) in the presence of a lithium salt ($LiClO_4$) at silica interfaces with nonlinear optical spectroscopic and electrochemical measurements. We further consider the role of the chirality (racemic vs. enantiomeric) on the properties of PC at this interface.

In recent experiments, we showed that acetonitrile creates a spatially organized structure at silica surfaces that is preserved even at high concentrations of inorganic salts, including $LiClO_4$, $NaClO_4$, $LiBF_4$, and $LiPF_6$.[7] The solvent arrangement is reminiscent of a supported lipid bilayer, such that

the cyano groups of the first sublayer of acetonitrile molecules point toward the silica surface, whereas molecules in the second sublayer tend to have cyano groups pointing toward the bulk solution.[8] The methyl groups of the two sublayers are interdigitated in a hydrophobic region. The bilayer-like organization is repeated with decreasing fidelity over a few nanometers into the solution. Through electrokinetic experiments, vibrational sum-frequency-generation (VSFG) spectroscopy, and molecular dynamics simulations, the solvent structure was found to direct the location of ions and to determine the effective potential of the interface.[7a] At low concentrations of ions, the interface is negatively charged, due to the cyano groups that point into the bulk liquid. However, at a threshold concentration that depends on the identity of the salt, the interface acquires a positive effective potential. The presence of negative and positive potentials was detected by recording the direction of electroosmosis in single pores.[7a, 9] These results underscore the importance of the solvent in the electrochemical properties of a solid–liquid interface and point to limitations in the ability of the classical electrical double layer model to describe interfaces involving some organic solvents.

Inspired by findings of spatial organization of acetonitrile and its role in the formation of the effective potential we considered additional questions. First, is interfacial solvent organization sensitive to the chirality of the solvent molecules? Second, if interfacial molecular structure is indeed affected by the solvent chirality, can these differences influence the interfacial potential? To answer these questions, we chose PC as our model system. PC is a chiral solvent whose enantiomerically pure forms are readily available commercially. Our first VSFG experiments with neat PC revealed that the arrangement of PC molecules on glass is indeed different for the racemic liquid and the enantiomerically pure liquid.[10] We also probed electrokinetic phenomena in pores in contact with $LiClO_4$ solutions in both types of PC, and concluded that the effective surface

potential induced by the racemic PC (which we henceforth denote as *rac*PC) is indeed higher than the potential induced by (*R*)-(+)-PC (which we henceforth denote (*R*)-PC).[10] These measurements, however, were not able to determine the magnitude of the potential, and moreover were recorded in salt concentration gradients, which made interpretation of the potential as a function of salt concentration difficult.

In this manuscript we quantify the effective interfacial potential in two types of pores in contact with $LiClO_4$ solutions prepared in *rac*PC and (*R*)-PC. VSFG characterization [7a, 10-11] of a quartz surface was performed over a wide range of $LiClO_4$ concentrations. These experiments reveal significant differences in the solid–liquid interfaces of *rac*PC versus (*R*)-PC solutions. The sign and magnitude of the interfacial potential were measured using glass nanopipettes with sub-100-nm diameters. The rectification properties in symmetric electrolyte concentrations[12] and the streaming current[3a, 13] were measured in this system. These experiments reveal that glass pipettes in contact with *rac*PC solutions exhibit higher positive potential than do glass pipettes filled with (*R*)-PC solutions of the same $LiClO_4$ concentration. Finally, we present measurements that probe the presence of the effective surface potential in pores prepared in polyethylene terephthalate (PET) films.[14] Similar to glass pipettes, the PET pores exhibit a higher interfacial potential when in contact with the solutions based on *rac*PC. Our work highlights the extreme sensitivity of the interfacial potential on the molecular organization of the solvent and underscores the need to develop a deeper understanding of chiral electrokinetic phenomena.

6.2. Materials and Methods

6.2.1. Chemicals

$LiClO_4$ (≥99.99% battery grade, Sigma Aldrich) and KCl (≥99.0% Sigma-Aldrich) were used as received. Racemic PC (99.7% pure HPLC Grade, Sigma Aldrich), and (*R*)-(+)-propylene carbonate (purity >98%, TCI chemicals) were used in the experiments. The chemicals were used as received. Aqueous solutions were prepared with Milli-Q water (resistivity = 18.2 MΩ·cm at 25 ºC, Thermo Scientific) and filtered with a 0.20-µm PVDF nylon syringe filter (MicroLiter).

6.2.2. VSFG measurements

The laser source for our VSFG setup is a 1 kHz, Ti-sapphire, regenerative amplifier (Coherent Legend Elite), which generates 800-nm, 80-fs pulses and has an average power of 3 W. The amplifier is seeded by a 76-MHz, Ti-sapphire oscillator (Coherent Mira) that is pumped with 5.2 W of the output of a continuous wave, 532-nm laser (Coherent Verdi-12) laser. The amplifier is pumped by a 1-kHz, Q-switched, frequency-doubled, Nd:YLF laser (Coherent Evolution). The amplifier output is directed through a 30/70 beam splitter, after which ~1 W of the output is sent to the mid-IR-generating path and the remaining 2 W to the 800-nm probe path. The former path includes optical-parametric amplifier and difference-frequency-generation modules (TOPAS, Light Conversion) that produce an IR beam with a bandwidth of 250 cm^{-1}, centered for the experiments reported here at 2945 cm^{-1}, with a maximum pulse energy of 15 mJ. The IR beam excites vibrations in the C–H stretching region of the spectrum.

The probe-beam portion of the amplifier output is spectrally narrowed using a 4*f* pulse stretcher with a slit, which reduces the bandwidth to ~5 cm^{-1}, after which the pulse energy is ~15 mJ. The probe beam then traverses a delay line. The IR and probe beams meet at the sample in a counterpropagating geometry, with incident angles of 61° and −58° from the surface normal, respectively. The signal is generated at an angle of −32.8° and is collected using a spectrometer (ActonSP300i) with a thermoelectrically cooled CCD camera (Spec-10:100, Roper Scientific). The experiments were performed in the *SSP* polarization configuration, with the polarizations listed in the order of the signal, probe, and IR. *P* denotes polarization in the plane of incidence and reflection, such that there is a projection of the polarization along the surface normal. *S* denotes polarization perpendicular to the plane of incidence and reflection, and therefore perpendicular to the surface normal. Eight 120-s scans were performed for each sample. The individual spectra were normalized to the nonresonant SFG signal from a gold substrate. A polystyrene film placed in the path of the IR beam while measuring the gold SFG signal was used to calibrate the frequency of the signal, using four of the polystyrene absorption peaks.

The cuvettes used for the VSFG studies were composed of IR-grade quartz (FireflySci). Before use, the cuvettes were rinsed sequentially with contaminant-free methanol, de-ionized water, and then acetone. The cuvettes were then oven-dried and placed in an oxygen plasma cleaner (Herrick) for 3 min.

6.2.3. Preparation of quartz nanopipettes

Nanopipettes were pulled from quartz capillaries (Q100-70-7.5, Sutter Instrument) with a CO_2-laser puller (P-2000, Sutter Instrument) to fabricate single barrel nanopipettes. A typical set of program parameters used was: Heat, 640; Velocity, 3; Filament, 40; Delay time, 180; and Pull, 155. The pipettes were characterized by scanning electron microscopy (FEI Quanta-FEG), which revealed a typical inner diameter of 72 ± 2 nm and an outer diameter of 104 ± 5 nm, as shown in Figure S1.

6.2.4. Preparation of pores in poly(ethylene) terephthalate (PET) films.

Single pores were fabricated in PET membranes using the track-etching technique.[14a] This method involves irradiation of a 3-cm-diameter, 12-µm-thick PET film using single, heavy, energetic (11.4 MeV/µ) ions, such as Xe, Au, or U (UNILAC, Universal Linear Accelerator at the Institute for Heavy Ions Research, Darmstadt, Germany), leading to the formation of a single damage track. A 100-µm-diameter metal mask located in front of the film, combined with adjustment of the ion beam to allow only one heavy ion to pass through the mask's aperture, allows for the creation of a single pore. The ion beam is shut down when an ion detector located on the opposite side of the film registers an event.[15] The films were then exposed to 365-nm light for 1 h on each side using a 115-V, UVGL-25 compact UV lamp (UVP, LLC), to ensure a more homogenous etching along the heavy-ion track.[16] Following the UV treatment, the films were subjected to wet chemical etching in 2 M NaOH at 60 °C.[14b] PET pores prepared by the track-etching method under the described conditions have been shown to exhibit symmetric and cylindrical shape, with an average pore diameter that increases linearly with chemical-etching time. The diameter of single PET pores were determined electrochemically by measuring the pore

resistance in a 1 M aqueous KCl solution, as reported previously.[9b] These high ionic strength conditions assure that the pore volume is filled with the bulk solution and that surface-charge effects are screened.

6.2.5. Electrokinetic and streaming-current measurements

Quartz nanopipettes

For nanopipette experiments, a two-electrode system was used to perform current–voltage (I–V) measurements with a picoammeter/voltage source (Keithley 6487, Keithley Instruments). A back-inserted Ag/AgCl wire inside the nanopipette served as the working electrode, and an Ag/AgCl pellet was placed in the bath solution which served as the reference electrode. The potential was ramped from -3 V to 3 V at 0.2 V/s. For streaming-current measurements in nanopipettes, a Ag/AgCl wire was back-inserted into the pipette, and a second Ag/AgCl electrode was placed in the bath solution. Current–time traces were measured with the headstage of an Axopatch 200b current amplifier (Molecular Devices) with a gain of 1 mV/1pA and a low-pass filter set to 1 kHz (-3 dB, 4 pole Bessel). Current was recorded at a sampling frequency of 50 – 100 kHz, using a low-noise data-acquisition system and pClamp 10.6 software (Axon Digidata 1440A, Molecular Devices). Pressure application through the side arm of the electrode holder (Warner Instruments) was performed with a high-speed pressure clamp (ALA Scientific) and was controlled through a pClamp protocol. The pressure protocol stepped in increments of 50 mm Hg that were each held for a duration of 8 s, then returned to 0 mm Hg after each step, before proceeding to the next increment. The current recorded during the 140 ms prior to each pressure step (i.e., at 0 mm Hg) was averaged and used as the initial current value (I_i). During a pressure step, the ion current was

measured for a duration of 1 s, and an averaged value was calculated as the streaming-current (I_{str}) value for each pressure. The change in the measured current, $\Delta I = I_{str} - I_i$, was determined for each pressure step.

Single pores in PET

Electrokinetic measurements with polymer membranes were performed using a home-made conductivity cell in which the single-pore membrane was mounted between two chambers filled with different concentrations of $LiClO_4$ in PC, which we denote c_{high} and c_{low}. Current–voltage curves were recorded with a Keithley 6487 picoammeter/voltage source (Keithley Instruments), with pellet Ag/AgCl electrodes serving as the working and reference electrodes in their respective chambers of the solution. The instrument was controlled using software written in LabVIEW (National Instruments). The voltage was varied between -2 V and +2 V in 0.1 V steps. Each PET membrane was exposed to 0.1 mM/1 mM, 0.5 mM/5 mM, 1 mM/10 mM, and 10 mM/100 mM concentration gradients of $LiClO_4$ prepared in *rac*PC or (*R*)-PC. Before switching salt concentrations, both chambers of the conductivity cell were rinsed thoroughly in neat solvent. For consistency, the ground electrode was always placed in the lower-concentration solution, and the working electrode was always placed in the higher-concentration solution. All current–voltage curves reflect average values and standard deviations from at least three forward and three reverse scans.

Streaming-current measurements were performed on PET pores using a home-made conductivity cell, modified with a custom hydrostatic-pressure setup. The single-pore membrane was mounted between two chambers containing an electrolyte solution with the same concentration. One side of the membrane was exposed to atmospheric pressure and contained a pellet Ag/AgCl electrode

submerged in the solution; this electrode served as the reference electrode. The other side of the membrane was airtight, and hydrostatic pressure was applied by manually varying the height of the liquid column via a system of plastic tubing. This side of the membrane also included a pellet Ag/AgCl electrode, which served as the working electrode. An Axon Instruments Axopatch 200B integrated patch clamp combined with a 1322A Digidata acquisition system (Molecular Devices) was used to record I_{str}. The hardware was operated in the whole-cell model ($\beta = 1$) employing a 1 kHz, low-pass Bessel filter, and I_{str} was sampled at a frequency of 1 kHz. The ion current at each applied pressure was measured for 15 s, and the values were subsequently averaged over time.

In both the membrane and pipette measurements, ambient electrical noise was minimized by use of a Faraday cage (Warner Instruments for the membranes and a home-built cage for the pipettes). Vibrational noise was reduced with a vibration-cancellation table (TMC for the membranes and Herzan for the pipettes). The ion current was recorded as a time series and was analyzed using Clampfit (Molecular Devices) and Igor Pro (Wavemetrics, Lake Oswego, OR, USA).

6.3. Results and Discussion

6.3.1. VSFG characterization of the solid–liquid interfaces of quartz and *rac*PC and (*R*)-PC solutions of $LiClO_4$

VSFG spectroscopy is especially well-suited to probe solid–liquid interfaces, because this technique is sensitive to molecular arrangements at interfaces at which centrosymmetry is broken.[17] We used this approach previously to probe the molecular structure of an interface created by quartz in contact with $LiClO_4$ solutions in acetonitrile (MeCN).[7] We found that the lipid-bilayer-like organization of MeCN at this interface is largely preserved in 1 M $LiClO_4$.[7a]

Due to the spatial organization of MeCN at this interface, lithium ions were found first to accumulate on the surface of the second sublayer to neutralize the partial negative charge on the nitrogen atoms in the cyano groups. Only at a threshold concentration of ~1 mM $LiClO_4$ could anions begin to enter the bilayer, allowing lithium to accumulate at the silica and outer bilayer surfaces to render this interface effectively positively charged.[7a]

PC also has a large dipole moment (~4.9 D), and the partial negative charge on the carbonyl oxygen can attract Li^+ ions to fulfill electroneutrality if PC molecules create organized bilayers. Based on the VSFG data for neat *rac*PC,[10] as well as on molecular dynamics simulations of the organization of *rac*PC on a positively-biased graphite electrode[18], this solvent is expected to create a structure on silica that is similar to those observed for MeCN[7a, 8, 19] and propionitrile.[5b, 20] We hypothesized that, as is the case for MeCN, the interfacial organization of PC molecules determines the ionic distribution and the effective potential. Here we use VSFG to probe the solvent organization as a function of electrolyte concentration at a quartz surface in contact with $LiClO_4$ solutions in both types of PC.

Figure 6.1 compares VSFG spectra recorded for $LiClO_4$ solutions in *rac*PC and (*R*)-PC. Due to the limited signal-to-noise ratio in the (*R*)-PC solutions, we show Gaussian-fitted spectra of both types of solutions to facilitate comparison; the raw data are presented in Figure S2. Reliable fitting was not possible at the highest concentrations of $LiClO_4$; thus we show fitted spectra only up to 10 mM and 0.1 mM $LiClO_4$ for *rac*PC and (*R*)-PC, respectively.

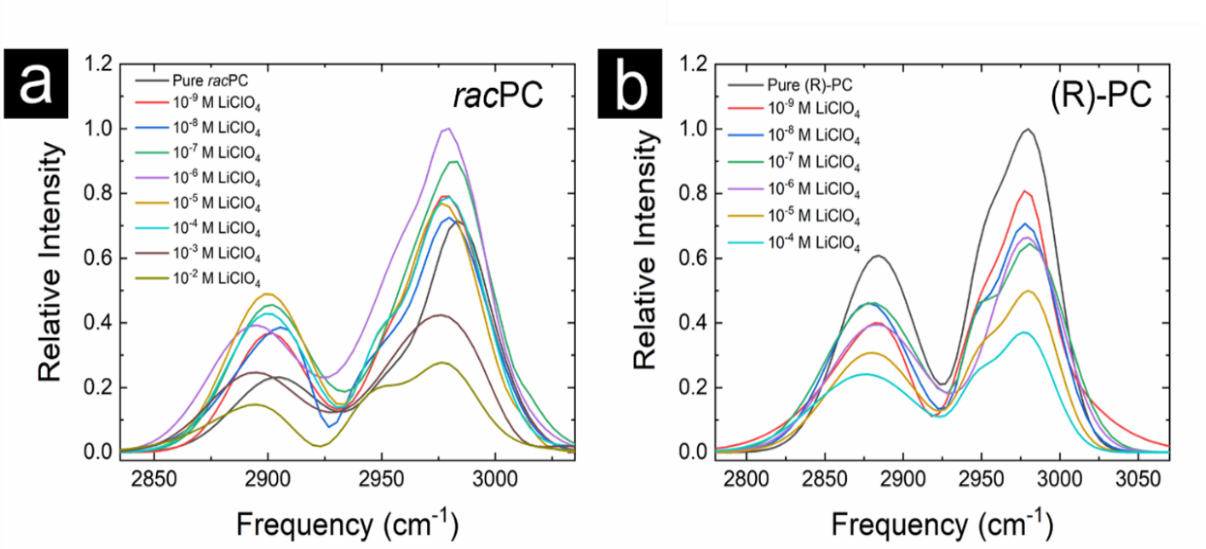

Figure 6.1. Gaussian fits to VSFG spectra for $LiClO_4$ prepared in (a) *rac*PC, and (b) (*R*)-PC. The raw spectra are presented in Figure S2. The spectra were normalized with respect to the highest signal recorded at 10^{-6} M $LiClO_4$ in (a) and with respect to the neat (*R*)-PC in (b).

The two broad peaks observed in the VSFG spectra in Figure 6.1 are attributed to symmetric C-H stretches of the methyl, methylene, and methine groups (~2920 cm^{-1}) and asymmetric C-H stretches of the methyl and methylene groups (~2980 cm^{-1}).[10] The concentration-dependent behavior of the spectra for the racemic solutions are similar to those for acetonitrile,[7a] with the asymmetric stretch intensity increasing up to a concentration of 10^{-6} M and the symmetric stretch intensity increasing up to a concentration of 10^{-5} M of $LiClO_4$ before decreasing at higher concentrations. These data indicate that the lipid-bilayer-like organization of *rac*PC causes cations to partition to the outside of the bilayer until the effective charge of the carbonyl oxygens has been neutralized. The partial negative charges on the carbonyl groups act as an electrostatic barrier that prevents anions from entering the bilayer, and the bilayer itself is compact enough to make it energetically unfavorable for cations to partition to the silica surface until anions can also enter the bilayer. The increase in the VSFG intensity at low concentrations of $LiClO_4$ indicates that the

presence of Li^+ at the outside of the bilayer changes the orientational distribution of the *rac*PC molecules in the second sublayer. Raman non-coincidence effect studies have shown that the carbonyl groups of PC molecules tend to dipole pair in the bulk liquid,[21] and it might therefore be expected that the carbonyl groups of PC molecules in the second sublayer dipole pair with those of adjacent molecules in the bulk liquid. The presence of cations should disrupt such ordering, which may account for the change in preferred orientation that leads to the increase in the VSFG intensity.

Once the outside of the surface bilayer of *rac*PC has been neutralized, it becomes energetically favorable for cations to partition to the surface and anions to partition into the bilayer, and the VSFG intensity begins to decrease, reaching half of its peak value at an electrolyte concentration of 10^{-3} M. In our previous studies of electrolyte solutions in MeCN,[7a] we noted that perchlorate is a large anion with delocalized charge, and so can be considered to be relatively hydrophobic, although some hydrogen bonding from surface silanol groups was also observed. However, the carbonyl carbon in PC is bonded to three different electron-withdrawing atoms, and so carries nearly a full positive charge.[22] We therefore expect that there will be strong interactions between the carbonyl carbons in each sublayer and any perchlorate ions that are inside of the bilayer. These interactions will have a strong impact on the organization of the interfacial solvent, leading to the observed decrease in the VFSG intensity at higher concentrations of $LiClO_4$. Taken together, our observations suggest that $LiClO_4$ in *rac*PC can induce effective positive charge at a silica interface at significantly lower concentrations than observed in solutions of $LiClO_4$ in MeCN.

The VSFG spectra for $LiClO_4$ in (*R*)-PC solutions differ markedly from those recorded in *rac*PC solutions (Figure 6.1b). In (*R*)-PC, the signal decreases monotonically with increasing concentration over the entire examined range of $LiClO_4$ concentrations, reaching half of the peak

value at 10^{-5} M. To rationalize this result, we note that manufacturer's reported data suggest the density of bulk (*R*)-PC at 25 °C (1.189 g/mL) is about 1 % less than that of *rac*PC (1.204 g/mL).[23] This difference can be a manifestation of possible packing constraints imposed on (*R*)-PC by only having a single enantiomer. The free volume in bulk (*R*)-PC could therefore be substantially larger than that in bulk *rac*PC. These effects should be recapitulated in the surface bilayer of (*R*)-PC. Although the organization of the first sublayer may be determined largely by the surface silanol groups with which the (*R*)-PC molecules hydrogen bond, the second sublayer is expected to be considerably more disordered than in the case of *rac*PC, explaining why the VSFG signal for neat (*R*)-PC at the silica interface is substantially larger than that for *rac*PC.[10]

We hypothesize, a larger free volume in the surface bilayer of (*R*)-PC allows cations to partition to the silica surface even at low concentrations of $LiClO_4$, influencing the organization of the first sublayer, and causing the VSFG signal to drop. The perchlorate anions are considerably larger than the lithium cations, but likely can also enter the bilayer even at low concentrations, as the electrostatic barrier of the second sublayer will be weaker than in *rac*PC. The presence of lithium ions at the silica surface will also create a driving force for anions to enter the bilayer.

VSFG measurements revealed that molecular organization at the quartz–PC interface is sensitive to whether the solvent is racemic or enantiomerically pure. Below, we use electrochemical approaches to probe the presence and magnitude of the interfacial surface potential as a function of $LiClO_4$ concentration in both types of PC. We first describe experiments using quartz pipettes,

in which the surface chemistry at the walls of the pipette is chemically similar to that of the quartz surfaces used for spectroscopic experiments.

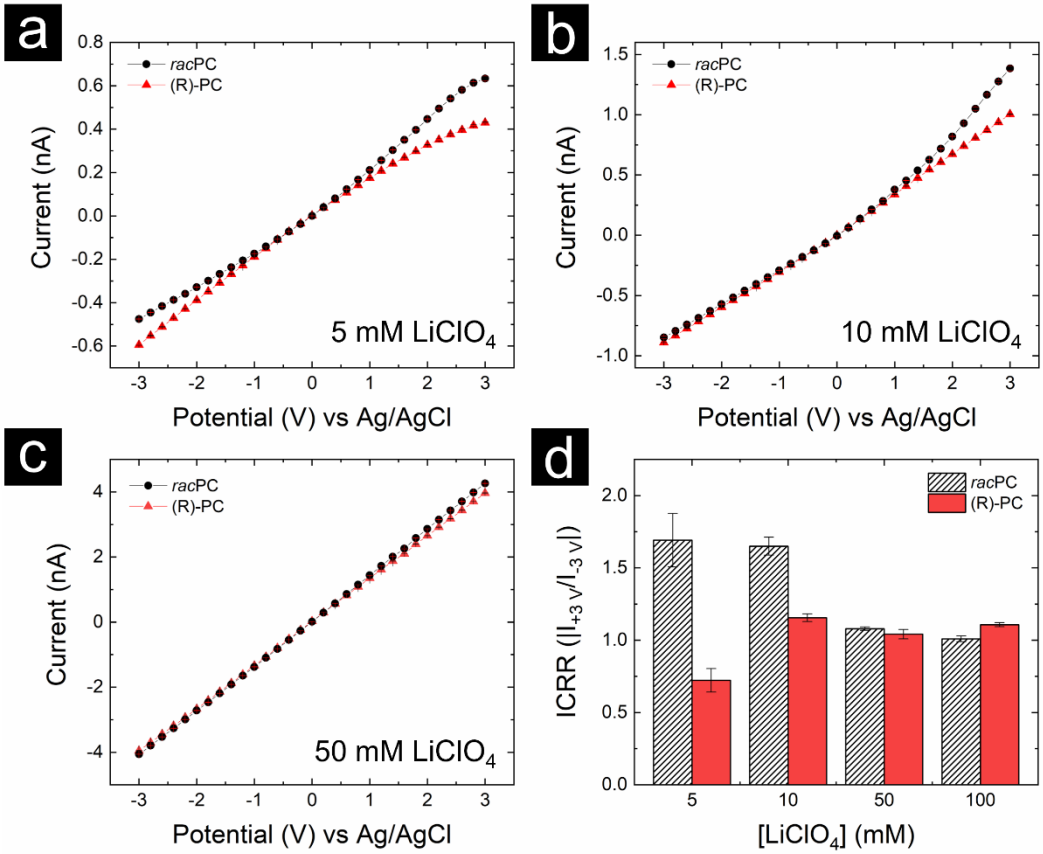

Figure 6.2. Current–voltage response of quartz nanopipettes filled with *rac*PC and (*R*)-PC with $LiClO_4$ concentrations of (a) 5 mM, (b) 10 mM, and (c) 50 mM. Note the identical currents recorded at low voltages for both types of solutions at each $LiClO_4$ concentration, in agreement with nearly identical ionic conductivities of racemic and enantiomeric PC solutions.[1] (d) Calculated ion–current rectification ratio at ±3 V for different electrolyte concentrations.

6.3.2. Electrochemical properties of nanopipettes in $LiClO_4$ solutions in *rac*PC and (*R*)-PC

Quartz pipettes pulled to small diameters provide a versatile platform for probing interfacial charge. The asymmetric conical structure of the pipette tip, combined with a relatively small opening diameter (<100 nm), results in transport properties that are dominated by the interplay among the glass surface, the geometry of the pipette, and the electrolyte solution. The asymmetry of the shape of the pipette, combined with the presence of the finite surface potential, results in asymmetry in transport of ions at the pipette opening. These effects have been widely exploited in sensing and imaging experiments.[24] Here, we use nanopipettes to measure ion currents induced by applied potentials and pressures.

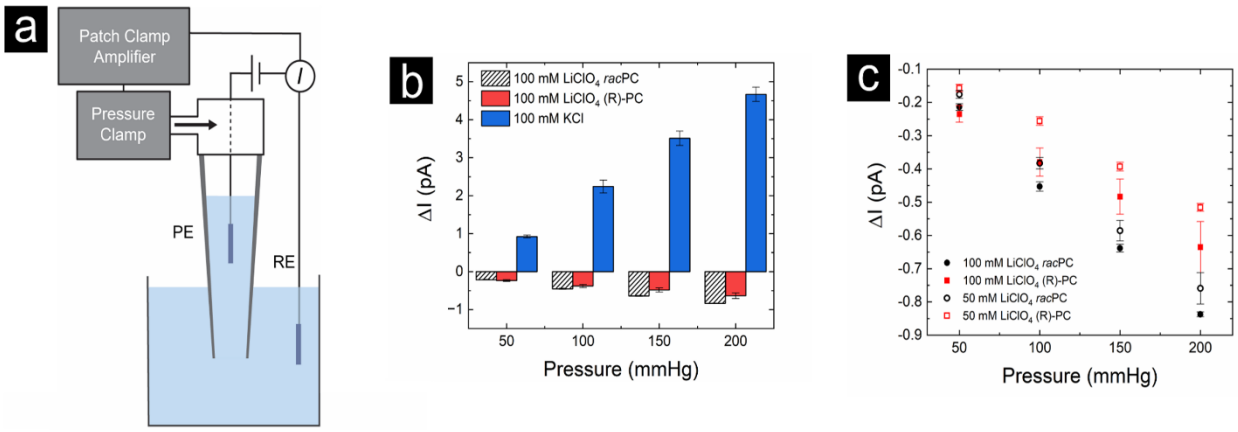

Figure 6.3. (a) Schematic for streaming-current measurements in quartz nanopipettes. (b) The streaming current (ΔI) as a function of applied pressure for pipettes filled with *rac*PC and (*R*)-PC with 100 mM $LiClO_4$, and with 100 mM KCl in water. (c) The streaming current as a function of applied pressure for 50 mM and 100 mM $LiClO_4$ solutions.

For the experiments described here, a symmetric ion concentration was employed on each side of the nanopipette, providing a direct measurement of ion transport, analogous to typical current–voltage measurements in nanopores. The combination of conical geometry and the presence of surface charge results in a voltage-polarity-dependent number of charge carriers in the pore, and a

voltage-polarity-dependent magnitude of the ion current, recorded as ion current rectification.[12b, 24d, 25] [12a] The measured current–voltage curves are therefore characterized by a ratio of currents recorded at the same magnitudes of voltage but opposite polarities. In our electrode configuration, pipettes in contact with aqueous salt solutions rectify such that negative currents are larger than positive currents. This behavior is expected, based on the presence of silanol groups on the pipette walls. On the other hand, if a pipette is chemically modified and positively charged, its I–V curves will be inverted, such that currents at positive voltages will be higher.[12c, 24d] Numerically, this behavior can be quantified via the absolute value of the ratio of the ion currents at two equivalent applied positive and negative potentials (here with a magnitude of 3 V), which is referred to as the ion–current rectification ratio (ICRR):[26]

$$ICRR = \left|\frac{I_+(+3V)}{I_-(-3V)}\right| \quad \textbf{Equation 1}$$

For the experiments shown here, ICRR > 1 (ICRR < 1) indicates presence of positive (negative) surface charges.

The current–voltage responses of nanopipettes in *rac*PC and (*R*)-PC as a function of $LiClO_4$ concentration are shown in **Figure 6.2(a-c)**, and the calculated ICRR at ±3 V is shown in **Figure 6.2d**. To minimize pipette-to-pipette variation, a single capillary was pulled into two nominally identical pipettes, which we refer to as "sister" pipettes. One sister pipette was filled with a $LiClO_4$ solution in *rac*PC, and the second sister pipette was filled with a $LiClO_4$ solution of identical concentration in (*R*)-PC. The nominal inner diameter of the pipettes used to collect data was 72 ± 2 nm, as characterized by SEM. For the lowest electrolyte concentration (5 mM), the results for *rac*PC and (*R*)-PC differed, with *rac*PC exhibiting an ICRR > 1 and (*R*)-PC exhibiting an ICRR <

1, which suggests a nominal positive charge in *rac*PC and a nominal negative charge in (*R*)-PC. At a 10 mM electrolyte concentration, both *rac*PC and (*R*)-PC exhibit ICRR > 1, suggesting a nominal positive charge. We note that the pipettes did not undergo any chemical modification, implying that the positive charge results from the arrangement of solvent molecules and ions at the interface. The magnitude of the ICRR in 10 mM $LiClO_4$ is, however, significantly higher in *rac*PC (~1.7) than in (*R*)-PC (~1.2). These observations are consistent with our earlier findings in polymer and silicon nitride pores, in which a lower magnitude of the effective surface potential in (*R*)-PC solutions was observed at similar concentrations.[10] Finally, for even higher concentrations (50 and 100 mM), the ICRR is close to 1 for both types of PC, suggesting that the pipettes either become near neutral, or that the surface charges are screened by the high salt concentration. Linear current–voltage curves for conically-shaped and charged pores are indeed recorded at concentrations above a threshold salt concentration at which the ion concentrations in the pores are no longer regulated by the presence of a surface potential.[12a, 27] In such a case, the lack of rectification is not indicative of a lack of finite surface charge, but rather points to effective screening of the charges by ions in the solution. The results shown here are in qualitative agreement with results from multiple sets of sister pipettes tested.

To probe the presence and magnitude of the surface charge at the higher concentrations of 50 mM and 100 mM, we employed the electrokinetic approach of measuring the streaming current, which is known to be dependent on the zeta potential at the surface.[3a] The zeta potential is the potential at a shear plane that is located some distance from the surface, and is often assumed to be the potential at the plane of the Stern layer. In the case of solid–liquid interfaces with a layered solvent, we expect that the shear plane will be positioned beyond the first bilayer. The streaming-current measurements entail placing a pipette in contact with the same solution on both sides, setting the

transmembrane potential to 0 V, and recording ion current upon gradual increments of the pressure difference across the pipette. The measured streaming current is carried by the counterions at the interface. The streaming current is positive (negative) when the interface has an effective negative (positive) potential.[13] The streaming current is dependent on the zeta potential of the interface, providing a direct probe of the magnitude and sign of the zeta potential.

Streaming-current measurements for sister pipettes in *rac*PC and (*R*)-PC were recorded for applied pressures in the range of 0-200 mmHg, with a patch-clamp configuration typically used for patching cell membranes (**Figure 6.3a**). In these measurements, differences between the current at zero pressure and applied pressures (streaming currents) were at the limit of instrumental noise, which only allowed for recording of the changes in current as a function of pressure for 50 mM and 100 mM solutions of $LiClO_4$.

Streaming-current measurements in a quartz nanopipette filled with 100 mM KCl are shown in **Figure 6.3b** for reference. Glass surfaces are known to have a net negative charge at pH > 3, resulting in a positive streaming current, in agreement with previous observations.[28]

For *rac*PC and (*R*)-PC solutions of $LiClO_4$, consistent trends are observed for each condition. In accordance with expectation, over the range investigated, the streaming current increases as a function of the applied pressure for both solutions in a monotonic manner. The streaming currents for the 50 mM and 100 mM solutions are negative, providing evidence that the pipettes have an effective positive surface charge at higher electrolyte concentrations. The streaming current is slightly larger for the 100 mM concentration than for the 50 mM concentration, suggesting that the zeta potential in the higher concentration might be higher. Finally, *rac*PC has higher negative streaming current values than does (*R*)-PC.

To calculate the magnitude of the zeta potential from streaming currents, we would need to model pressure-driven flow in glass pipettes together with local ionic concentrations at the solid–liquid interface. A simpler approach to zeta potential in PC solutions utilizes literature values of zeta potentials of glass in aqueous solutions. The zeta potential of glass in ~100 mM KCl is approximately -30 mV.[29] Thus, if the magnitude of the zeta potential in PC is similar to that in water, the streaming current in PC would be ~3 times lower due to the higher dynamic viscosity of the organic solvent. The data in Figure 3 indicate that the magnitude of streaming currents is at least 5 times lower in PC than in water, so we estimate that the magnitude of the zeta potential is +20 mV in *rac*PC, and +15 mV in (*R*)-PC.

These electrokinetic measurements complement conclusions made based on I–V curves. In particular, the effective surface charge of glass pipettes in contact with 50 mM and 100 mM $LiClO_4$ solutions remains positive in both types of PC solutions. However, the magnitude of the surface charge is higher in *rac*PC. The measurements also allowed us to conclude that the differences in the molecular arrangement at the interface in *rac*PC and (*R*)-PC observed at low salt concentrations through I–V curves (**Figure 6.3**) are preserved at high salt concentrations.

The measurements with quartz pipettes are also in agreement with the VSFG spectra of a quartz surface in contact with PC electrolyte solutions (**Figure 6.1**). The *rac*PC can create a more organized layered structure at the interface, changing the ability of cations and anions to enter the surface bilayer.

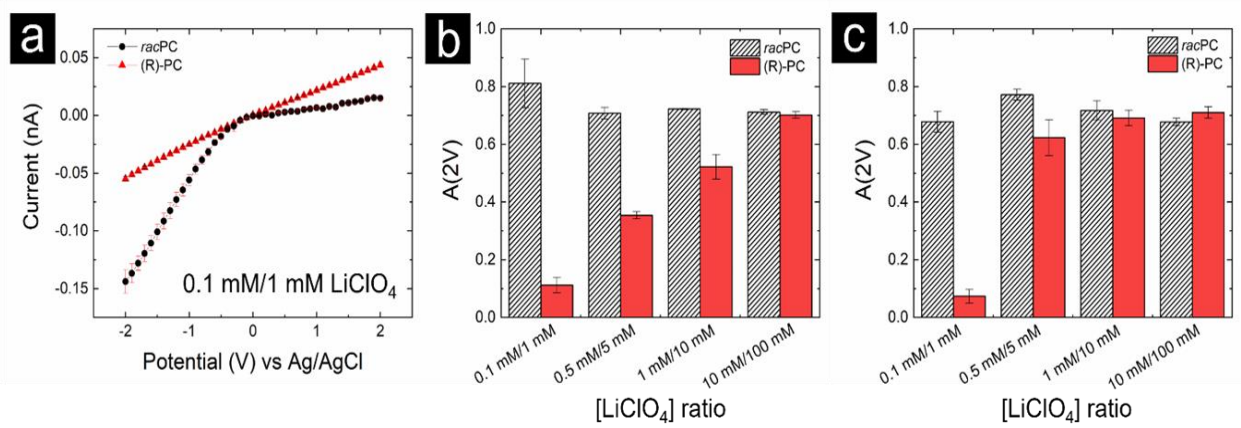

Figure 6.4. Electrochemical data for single PET pores. (a) I–V curves for a 390-nm-diameter pore when in contact with a 0.1 mM/1 mM concentration gradient of $LiClO_4$ prepared using either *rac*PC or (*R*)-PC. (b) Bar graph summarizing the ion-current anisotropy, *A*(2V), data for a range of concentration gradients. (c) Bar graph summarizing *A*(2V) data for a single, 450-nm-diameter PET pore.

Accumulation of anions within the bilayer, as indicated by the VSFG spectra, leads to a local accumulation of lithium ions and formation of the effective positive surface charge in all probed $LiClO_4$ concentrations in *rac*PC. The layered structure for (*R*)-PC-based solutions is less organized and has greater free volume, such that the accumulation of lithium ions, and the resulting positive charge, is weaker.

6.3.3. Single PET pores exhibit an effective surface potential that is dependent on the form of PC

The chirality-dependent interfacial potential was also tested in single pores in a polyethylene terephthalate (PET) film exposed to $LiClO_4$ solutions in *rac*PC and (*R*)-PC. PET pores prepared by the track-etching technique contain a high density of carboxylic acid groups.[30] We predict that the carbonyl groups in PC will accept hydrogen bonds from the carboxylic acid groups, similar to what is observed for silanol groups in silica.[10] Consequently, PC is also expected to create a layered structure near a PET surface.

To test the presence and polarity of interfacial potential on PET pores, we used a different method than the one applied for the glass pipettes. The approach used is applicable to pores of any diameter, and enables detection of surface charge even in large pores and at high electrolyte concentrations. Instead of conically-shaped nanopores, we prepared cylindrically-shaped pores with an opening a few hundred nanometers in diameter.[9] Such single-pore membranes were placed between two electrolyte solutions with different concentrations, c_{low} and c_{high}. This situation naturally leads to ion-current rectification when the interface exhibits a non-zero potential. By construction, with the ground electrode placed in the chamber with c_{low}, it can be deduced that when the interface carries an effective negative potential, the direction of electroosmosis will be determined by the cations. For example, for positive applied voltages, the cations will electroosmotically drag the solution with c_{high} into the pore, and for negative applied voltages, the pore will be filled with the solution with c_{low}. Therefore, a pore with negative surface potential will exhibit asymmetric current-voltage curves such that $|I(+V)| > |I(-V)|$. A pore with positive surface charges, on the other hand, will lead to asymmetric I–V curves with $|I(+V)| < |I(-V)|$. A complete, in-depth explanation of the influence of electroosmosis in the electrical setup has been given previously.[10] The polarity of the surface potential of pores can thus be easily deduced from the characterization of I–V curves recorded under an electrolyte concentration gradient.

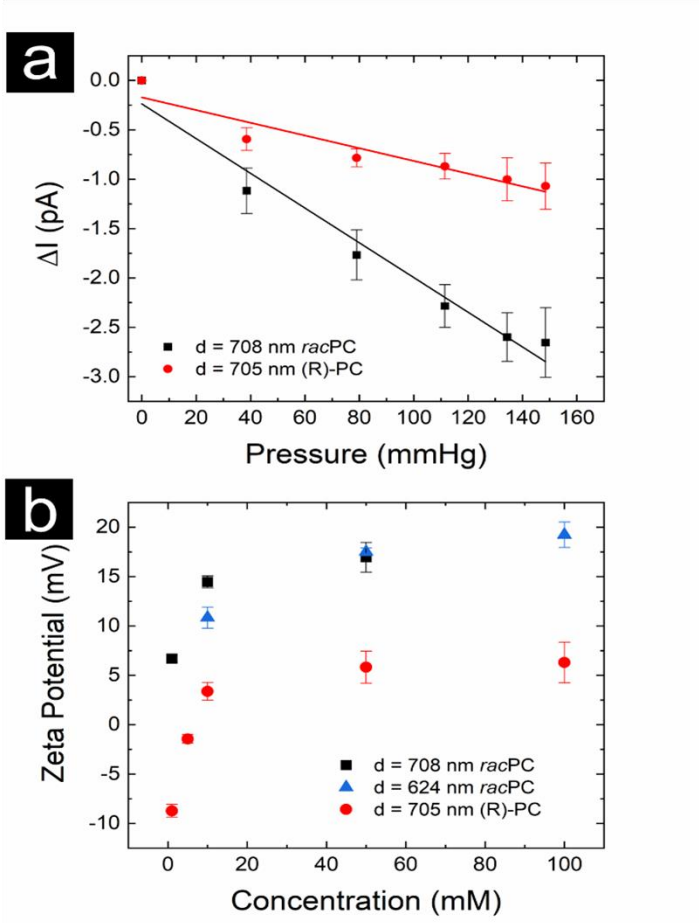

Figure 6.5. (a) Streaming current through single PET pores with an opening diameter of ~700 nm recorded in 50 mM $LiClO_4$ in *rac*PC and (*R*)-PC. (b) Calculated zeta potentials as a function of the concentration of $LiClO_4$. Data for three single PET pores of different diameters (*d*) are reported.

All I–V curves were described by the ion current anisotropy, *A*(V), defined previously as[7a, 10]:

$$A(V) = \frac{I(-V)+I(V)}{I(-V)-I(V)}$$ **Equation 2**

By the defined convention, a positive effective surface potential leads to a positive value of *A*(V), and vice versa. The magnitude of *A*(V) is an indirect measure of the magnitude of the surface potential, i.e. pores with larger surface potentials produce I–V curves that are more asymmetric, because pores with lower (higher) interfacial potential will be filled less (more) completely with a

solution of either side, leading to lower (higher) *A*(V). Note that the origin of rectification and a non-zero ion-current anisotropy value here is different from the origin of the ICRR observed with nanopipettes (**Figure 6.2**).

Figure 6.4 a,b shows I–V curves and *A*(2V) for a single PET pore with a diameter of 390 nm. These measurements were performed with $LiClO_4$ solutions prepared using either *rac*PC or (*R*)-PC. Under the lowest concentration gradient, 0.1 mM/1 mM, the I–V curve for the *rac*PC solutions suggested that the pore exhibited a strong effective positive surface potential. However, when the same concentration gradient was used with (*R*)-PC, the I–V curves were effectively linear, indicating that the effective surface potential was close to zero. As the concentrations on both sides of the pore were increased, the pore began to rectify in the same direction in both *rac*PC and (*R*)-PC, until the largest concentration gradient, for which the I–V curves and values of *A*(2V) for both types of solutions became identical. These results agree well with our previous work.[10] Data for another, independently prepared pore, are shown in **Figure 6.4c**; this pore had transport properties in *rac*PC and (*R*)-PC that were qualitatively similar to the pore in **Figure 6.4 a,b**.

Although the ion-current anisotropy allows us to draw comparisons of effective surface potentials measured under different conditions, we cannot directly relate *A*(V) to the magnitude of the effective surface potential. To quantify the surface potential, we again turn to the electrokinetic method of measuring the zeta potential through recording streaming current.[3a, 31] Here, we use the relationship derived from combining the charge density distribution in the diffuse layer and the pressure-driven flow of the electrolyte in a microfluidic system. In our measurements and analysis, we use a relationship that was analytically determined for a cylindrical capillary using the Poisson-Boltzmann and Navier-Stokes equations.[3a, 31a] In this case, the streaming current, I_{str}, is

proportional to the applied pressure, *P*, with a proportionality constant that depends on the zeta potential, ζ:

$$I_{str} = -\frac{A\,\varepsilon_r\varepsilon_0}{\eta}\,\frac{P}{L}\,\zeta$$ **Equation 3**

This formula is valid in cases when the electrical double layer, or, more generally, the interfacial region with modified concentrations, is thin compared to the pore radius, which holds for our ~400-nm-diameter pores. Because we measured the streaming current as the pressure was slowly varied, we can use the slope of a linear fit to the current vs. pressure curve, $\Delta I_{str}/\Delta P$, when calculating ζ for each ionic concentration. A representative current vs. pressure curve, including a linear fit for extracting $\Delta I_{str}/\Delta P$, for 50 mM $LiClO_4$ in *rac*PC and (R)-PC is shown in **Figure 6.5a**. This approach has the advantage of being insensitive to a current offset, and being more precise than a measurement using a single pressure only. The diameter of each pore was measured electrochemically and used to calculate the cross-sectional pore area *A*. The channel length (*L* = 12 μm), as reported by the manufacturer, and tabulated values of the permittivity (ε_r = 64 at 25 °C, $\varepsilon_0 = 8.85 \times 10^{-12}$ F/m)[32] and the dynamic viscosity (η = 2.4 mPa·s at 25 °C)[33] were used to calculate values of ζ .

Figure 6.5 shows example streaming-currents and the cumulative zeta potential measurements for three different, single, PET pores of varying diameter at different concentrations of $LiClO_4$, prepared using *rac*PC and (*R*)-PC. When the membranes were in contact with solutions prepared using *rac*PC, the zeta potential at all concentrations was positive. When a membrane was in contact with solutions prepared using (*R*)-PC, the zeta potential for concentrations greater than 5 mM was also positive and followed a similar dependence on ionic concentration to that for *rac*PC, but with

a significantly lower magnitude. This behavior agrees with our electroosmosis results (**Figure 6.4**). Specifically, at the lowest concentration gradient studied, 0.1 mM/1 mM $LiClO_4$, the magnitude of *A*(2V) was nearly an order of magnitude smaller for (*R*)-PC than for *rac*PC. We also note that there is a visible dependence of the zeta potential on ionic concentration for both types of PC, which was not previously detected by our electroosmosis technique. Specifically, at 5 mM $LiClO_4$, (*R*)-PC has a zeta potential that is close to zero, and at 1 mM $LiClO_4$ the zeta potential is negative.

We return to our VSFG results (**Figure 6.1**) to gain further insights into the origin of the electrolyte- concentration-dependent zeta potential in both types of PC. We hypothesize that PC molecules create organized bilayers, similar to what has been observed for MeCN, and the partial negative charge on the carbonyl oxygen creates an inherently negative effective surface charge in the neat solvent.[7a, 10] Our VSFG data indicate that at low and moderate concentrations of $LiClO_4$ in *rac*PC, cations can partition to the exterior of the bilayer and neutralize the partial negative charge on the carbonyl oxygens in the second sublayer. At higher concentrations, the interface becomes positively charged due to anions partitioning into the bilayer and lithium ions accumulating at the exterior and at the silica surfaces. The zeta potential measurements for *rac*PC in **Figure 6.5** were obtained at concentrations well above the regime in which the VSFG data indicate that neutralization is achieved, and so the zeta potential is positive. We expect that if we were able to measure the zeta potential at a low enough concentration of $LiClO_4$ in *rac*PC, we would observe negative values.

Our VSFG results suggest that the surface bilayer in (*R*)-PC can be porous to ions even at the lowest concentrations measured, likely due to a larger free volume introduced by packing constraints. Accordingly, ions can partition into the bilayer even well before concentrations at which the charge on the exterior of the bilayer has been neutralized. The ability of anions to

partition into the bilayer even at low electrolyte concentrations allows the effective surface charge to remain negative up to a considerably larger electrolyte concentration than for *rac*PC. The zeta potential measurements for (*R*)-PC indicate that the negative surface charge persists up to a $LiClO_4$ concentration of approximately 5 mM.

The electrochemical properties of PC solutions in PET pores as studied using electroosmosis and ion-concentration gradients, as well as pressure differences and symmetric salt conditions, point to the same conclusion: the effective surface potential is dependent on whether *rac*PC or (*R*)-PC is used. There are, however, visible differences in the behavior of PC in PET pores probed with the two methods. Notably, at small concentrations, the zeta potential in (*R*)-PC is negative (**Figure 6.5**), in contrast to what is seen with the electroosmosis method (**Figure 6.4**). Additionally, there is a significant difference in magnitude of the positive zeta potential between *rac*PC and (*R*)-PC, which is not seen in the higher concentrations with the electroosmosis method. We propose that the nuances in the exact magnitudes of the effective surface charge may not have appeared in our electroosmosis experiments because these experiments are performed under a concentration gradient rather than at a uniform concentration. In addition, in the case of our symmetric pores, there might be a threshold effective surface potential that leads to complete filling of the pore volume with the solution from one side of the pore for one voltage polarity, and with the solution from the other side for the opposite voltage polarity. As a result, the ion-current anisotropy could reach its maximum value and stay constant even if the effective potential increased.

Qualitatively similar findings of a higher positive potential present on silica and polymer surfaces in contact with *rac*PC point to the universal character of our findings. Our results indicate that

electrochemical properties of solid–liquid interfaces are sensitive to the chiral state of the solvent even for surfaces that are not atomically flat.

6.4. Conclusions

Here we used nonlinear spectroscopic, electrochemical, and electrokinetic methods to probe and quantify the effective surface potential applicable to electrolyte solutions in PC. Two types of pores were used in the experiments, glass pipettes and polymer pores that were subjected to $LiClO_4$ solutions prepared in (*R*)-PC and *rac*PC. Current–voltage curves and streaming-current measurements pointed to the existence of finite effective surface charges in both types of pores that are dependent on the chiral form of the solvent and the electrolyte concentrations. The accompanying spectroscopic measurements revealed that the effective surface potential is determined by a bilayer-like structure of the solvent that dictates the position of ions, and that the possible additional free volume in (*R*)-PC in comparison to *rac*PC enables ions to penetrate the surface bilayer in the former liquid at all electrolyte concentrations studied here.

We typically think of the non-chirality-dependent physical properties of racemic and enantiomerically-pure versions of the same material as being identical. The work presented here shows that that viewpoint might not be correct. Our experiments indicate that differences in the packing density of *rac*PC and (*R*)-PC are reflected in strikingly different electrochemical and electrokinetic behavior at a polar interface. This work underscores the need to develop a deeper understanding of the role of chirality at solid–liquid interfaces and suggests new approaches for improving ion transport in applications that involve interfaces in polar, aprotic organic solvents.

6.5. References

(1) P. Jankowski, K. Grzegorzewska, A. Szabłowska, M. Piszcz, M. Dranka, G. Z. Żukowska, M. Kalita, *Electrochimica Acta* **2015**, *175*, 240-246.

(2) (a) H. B. Park, J. Kamcev, L. M. Robeson, M. Elimelech, B. D. Freeman, *Science* **2017**, *356*, eaab0530; (b) S. Sharma, P. Chand, *Results in Chemistry* **2023**, *5*, 100885; (c) P. Marchetti, M. F. J. Solomon, G. Szekely, A. G. Livingston, *Chemical Reviews* **2014**, *114*, 10735-10806; (d) R. Epsztein, R. M. DuChanois, C. L. Ritt, A. Noy, M. Elimelech, *Nature Nanotechnology* **2020**, *15*, 426-436; (e) S. Howorka, Z. Siwy, *Chemical Society Reviews* **2009**, *38*, 2360-2384; (f) L. Xue, H. Yamazaki, R. Ren, M. Wanunu, A. P. Ivanov, J. B. Edel, *Nature Reviews Materials* **2020**, *5*, 931-951; (g) R. P. Lively, D. S. Sholl, *Nature Materials* **2017**, *16*, 276-279; (h) M. J. Zachman, Z. Tu, L. A. Archer, L. F. Kourkoutis, *ACS Energy Letters* **2020**, *5*, 1224-1232; (i) Z. Zhu, D. Wang, Y. Tian, L. Jiang, *Journal of the American Chemical Society* **2019**, *141*, 8658-8669; (j) G. H. Pollack, *Adv Colloid Interface Sci* **2003**, *103*, 173-196; (k) F. M. Geiger, *The Journal of Physical Chemistry B* **2021**, *125*, 10401-10403; (l) K. N. Olafson, R. J. Clark, P. G. Vekilov, J. C. Palmer, J. D. Rimer, *ACS Applied Materials & Interfaces* **2018**, *10*, 29288-29298; (m) Y. Chen, L. Qing, T. Liu, S. Zhao, Y. Han, *Nano Energy* **2022**, *102*, 107660; (n) X. Su, *Current Opinion in Colloid & Interface Science* **2020**, *46*, 77-93; (o) B. Honig, A. Nicholls, *Science* **1995**, *268*, 1144-1149; (p) J. N. Israelachvili, in *Intermolecular and Surface Forces (Third Edition)* (Ed.: J. N. Israelachvili), Academic Press, San Diego, **2011**, pp. 291-340; (q) M. Tanaka, *Current Opinion in Colloid & Interface Science* **2013**, *18*, 432-439.

(3) (a) R. B. Schoch, J. Y. Han, P. Renaud, *Reviews of Modern Physics* **2008**, *80*, 839-883; (b) M. E. Davis, J. A. McCammon, *Chemical Reviews* **1990**, *90*, 509-521; (c) R. M. M. Smeets, U. F. Keyser, D. Krapf, M. Y. Wu, N. H. Dekker, C. Dekker, *Nano Letters* **2006**, *6*, 89-95; (d) A. Alcaraz, E. M. Nestorovich, M. Aguilella-Arzo, V. M. Aguilella, S. M. Bezrukov, *Biophysical Journal* **2004**, *87*, 943-957; (e) R. Qi, R. Luo, *Journal of Chemical Information and Modeling* **2019**, *59*, 409-420.

(4) (a) G. Feng, J. Huang, B. G. Sumpter, V. Meunier, R. Qiao, *Physical Chemistry Chemical Physics* **2010**, *12*, 5468-5479; (b) Y. Cui, T.-S. Chung, *Nature Communications* **2018**, *9*, 1426.

(5) (a) Z. Hu, J. D. Weeks, *The Journal of Physical Chemistry C* **2010**, *114*, 10202-10211; (b) S. Liu, Z. Hu, J. D. Weeks, J. T. Fourkas, *The Journal of Physical Chemistry C* **2012**, *116*, 4012-4018; (c) A. Mendhe, H. S. Panda, *Discover Materials* **2023**, *3*, 29; (d) D. Ren, S. Ren, Y. Lin, J. Xu, X. Wang, *Chemosphere* **2021**, *271*, 129425.

(6) (a) Z. P. Cano, D. Banham, S. Y. Ye, A. Hintennach, J. Lu, M. Fowler, Z. W. Chen, *Nature Energy* **2018**, *3*, 279-289; (b) L. S. Roselin, R. S. Juang, C. T. Hsieh, S. Sagadevan, A. Umar, R. Selvin, H. H. Hegazy, *Materials* **2019**, *12*; (c) M. S. Whittingham, *Nano Letters* **2020**, *20*, 8435-8437.

(7) (a) J. W. Polster, A. J. Souna, M. H. Motevaselian, R. A. Lucas, J. D. Tran, Z. S. Siwy, N. R. Aluru, J. T. Fourkas, *Natural Sciences* **2022**, *2*, e20210099; (b) A. J. Souna, M. H. Motevaselian, J. W. Polster, J. D. Tran, Z. S. Siwy, N. R. Aluru, J. T. Fourkas, *Physical Chemistry Chemical Physics* **2024**, *26*, 6726-6735.

(8) B. J. Berne, J. T. Fourkas, R. A. Walker, J. D. Weeks, *Accounts of Chemical Research* **2016**, *49*, 1605-1613.

(9) (a) R. A. Lucas, C.-Y. Lin, Z. S. Siwy, *The Journal of Physical Chemistry B* **2019**, *123*, 6123-6131; (b) Y. H. Qiu, R. A. Lucas, Z. S. Siwy, *Journal of Physical Chemistry Letters* **2017**, *8*, 3846-3852.

(10) S. Silva, S. Singh, E. Cao, J. T. Fourkas, Z. S. Siwy, *Faraday Discussions* **2023**, *246*, 508-519.

(11) C. A. Rivera, J. S. Bender, K. Manfred, J. T. Fourkas, *Journal of Physical Chemistry A* **2013**, *117*, 12060-12066.

(12) (a) C. Wei, A. J. Bard, S. W. Feldberg, *Analytical Chemistry* **1997**, *69*, 4627; (b) H. S. White, A. Bund, *Langmuir* **2008**, *24*, 2212; (c) S. Umehara, N. Pourmand, C. D. Webb, R. W. Davis, K. Yasuda, M. Karhanek, *Nano Letters* **2006**, *6*, 2486-2492; (d) T. Plett, W. Q. Shi, Y. H. Zeng, W. Mann, I. Vlassiouk, L. A. Baker, Z. S. Siwy, *Nanoscale* **2015**, *7*, 19080-19091.

(13) F. H. J. van der Heyden, D. Stein, K. Besteman, S. G. Lemay, C. Dekker, *Physical Review Letters* **2006**, *96*, 224502.

(14) (a) R. L. Fleischer, P. B. Price, R. M. Walker, R. M. Walker, *Nuclear Tracks in Solids: Principles and Applications*, University of California Press, **1975**; (b) S. Müller, C. Schötz, O. Picht, W. Sigle, P. Kopold, M. Rauber, I. Alber, R. Neumann, M. E. Toimil-Molares, *Crystal Growth & Design* **2012**, *12*, 615-621.

(15) R. Spohr, **1983**.

(16) P. Y. Apel, Y. E. Korchev, Z. Siwy, R. Spohr, M. Yoshida, *Nuclear Instruments and Methods in Physics Research Section B: Beam Interactions with Materials and Atoms* **2001**, *184*, 337-346.

(17) (a) M. Buck, M. Himmelhaus, *Journal of Vacuum Science & Technology A* **2001**, *19*, 2717-2736; (b) F. Vidal, A. Tadjeddine, *Reports on Progress in Physics* **2005**, *68*, 1095.

(18) L. Yang, B. H. Fishbine, A. Migliori, L. R. Pratt, *The Journal of Chemical Physics* **2010**, *132*, 044701.

(19) F. Ding, Z. Hu, Q. Zhong, K. Manfred, R. R. Gattass, M. R. Brindza, J. T. Fourkas, R. A. Walker, J. D. Weeks, *The Journal of Physical Chemistry C* **2010**, *114*, 17651-17659.

(20) F. Ding, Q. Zhong, K. Manfred, X. He, J. S. Bender, M. R. Brindza, R. A. Walker, J. T. Fourkas, *The Journal of Physical Chemistry C* **2012**, *116*, 4019-4025.

(21) A. Brodin, P. Jacobsson, *Journal of Molecular Liquids* **2011**, *164*, 17-21.

(22) M. I. Chaudhari, A. Muralidharan, L. R. Pratt, S. B. Rempe, *Modeling Electrochemical Energy Storage at the Atomic Scale* **2018**, 53-77.

(23) (a) Merck KGaA, Darmstadt, Germany and/or its affiliates., "Propylene carbonate", https://www.sigmaaldrich.com/US/en/product/sial/310328#product-documentation, (accessed 02 May 2024); (b) Merck KGaA, Darmstadt, Germany and/or its affiliates, "(R)-(+)-Propylene carbonate", https://www.sigmaaldrich.com/US/en/product/aldrich/540013, (accessed 02 May 2024)

(24) (a) G. Caniglia, G. Tezcan, G. N. Meloni, P. R. Unwin, C. Kranz, *Annual Review of Analytical Chemistry* **2022**, *15*, 247-267; (b) N. Sa, L. A. Baker, *Journal of the*

Electrochemical Society **2013**, *160*, H376-H381; (c) N. Sa, W. J. Lan, W. Q. Shi, L. A. Baker, *ACS Nano* **2013**, *7*, 11272-11282; (d) Z. S. Siwy, S. Howorka, *Chemical Society Reviews* **2010**, *39*, 1115-1132.

(25) (a) M. Ali, P. Ramirez, S. Mafé, R. Neumann, W. Ensinger, *ACSs Nano* **2009**, *3*, 603-608; (b) X. Hou, W. Guo, L. Jiang, *Chemical Society Reviews* **2011**, *40*, 2385-2401; (c) Z. Zhang, X. Huang, Y. Qian, W. Chen, L. Wen, L. Jiang, *Advanced Materials* **2020**, *32*, 1904351.

(26) (a) C. Wei, A. J. Bard, S. W. Feldberg, *Analytical Chemistry* **1997**, *69*, 4627-4633; (b) E. A. Heins, L. A. Baker, Z. S. Siwy, M. O. Mota, C. R. Martin, *The Journal of Physical Chemistry B* **2005**, *109*, 18400-18407; (c) Z. Siwy, E. Heins, C. C. Harrell, P. Kohli, C. R. Martin, *Journal of the American Chemical Society* **2004**, *126*, 10850-10851; (d) H. S. White, A. Bund, *Langmuir* **2008**, *24*, 2212-2218.

(27) J. Cervera, B. Schiedt, R. Neumann, S. Mafé, P. Ramírez, *The Journal of Chemical Physics* **2006**, *124*.

(28) D. C. Martins, V. Chu, D. M. F. Prazeres, J. P. Conde, *Microfluidics and Nanofluidics* **2013**, *15*, 361-376.

(29) (a) Y. Gu, D. Li, *Journal of Colloid and Interface Science* **2000**, *226*, 328-339; (b) M. Castelain, F. Pignon, J.-M. Piau, A. Magnin, *The Journal of Chemical Physics* **2008**, *128*.

(30) (a) A. Wolf, N. Reber, P. Y. Apel, B. E. Fischer, R. Spohr, *Nuclear Instruments and Methods in Physics Research Section B: Beam Interactions with Materials and Atoms* **1995**, *105*, 291-293; (b) M. R. Powell, I. Vlassiouk, C. Martens, Z. S. Siwy, *Physical Review Letters* **2009**, *103*, 248104.

(31) (a) L. Renaud, P. Kleimann, P. Morin, *Electrophoresis* **2004**, *25*, 123-127; (b) B. J. Kirby, E. F. Hasselbrink Jr., *Electrophoresis* **2004**, *25*, 187-202; (c) P. Saha, C. Nam, M. A. Hickner, I. V. Zenyuk, *The Journal of Physical Chemistry C* **2019**, *123*, 19493-19505.

(32) R. Payne, I. E. Theodorou, *The Journal of Physical Chemistry* **1972**, *76*, 2892-2900.

(33) N. Peruzzi, P. Lo Nostro, B. W. Ninham, P. Baglioni, *Journal of Solution Chemistry* **2015**, *44*, 1224-1239.

Chapter 7: Conclusions and future directions

It is vital to understand chemical processes occurring at liquid–solid interfaces, which are fundamental to countless applications, such as in the fields of energy storage, nanofluidic transport, and biological processes, including protein aggregation. Throughout this dissertation I have demonstrated that the electrical double-layer (EDL) model is insufficient for describing many systems involving polar, aprotic organic solvents. In particular, I have shown that an inherent limitation of the EDL model lies in this model's treatment of a solvent as a homogenous continuum and ions as point charges. Using VSFG spectroscopy to analyze the properties of polar, aprotic organic solvents near silica interfaces, I have extended the scope of previous results from our group that showed that solvent organization plays a significant role in the ordering of ions in MeCN.

Through my studies with different polar, aprotic organic solvents that undergo strong ordering near a silica interface, I have been demonstrated how changes in solvent structure, mixing of solvents, and solvent chirality can affect both the organization of a solvent and its interaction with ions. In Chapter 3 I showed how EtCN, which is chemically very similar to MeCN with just a single extra methylene group forms a differently packed surface bilayer to MeCN at the silica interface. The VSFG results indicate that ions can enter the bilayer at roughly an order of magnitude less concentration in EtCN compared to MeCN. We attribute this result to the greater compactness of the EtCN bilayer which allows it to expand more and let in more anions compared to MeCN.

In Chapter 4 I explored the organization of a solvent mixture at the liquid–solid interface. I demonstrated that in mixtures of EtCN and MeCN-d_3, each liquid preferentially partitions to a different sublayer of the surface bilayer. This discovery may help to shed light on the behavior of

interfacial systems with mixed solvents, such as lithium-ion batteries, potentially leading to strategies to improve performance.

In Chapter 5 I combined VSFG studies with electrokinetic measurements from our collaborators to reveal that propylene carbonate (PC) takes on an interfacial structure that is sensitive to the chirality of the solvent. At the silica interface, racemic PC creates a layered structure that is more ordered than that of enantiomerically pure PC. Results for both types of PC are also in strong contrast to the classic EDL picture, in which the solvent is treated as a homogeneous continuum. Our results also point to the potential for tuning ionic and fluidic transport with solvent chirality or using solvents that have other packing constraints.

In Chapter 6 I presented the results of experiments on electrolytes in chiral and racemic PC at a silica interface. VSFG measurements revealed that, as in MeCN, the bilayer-like interfacial structure of PC dictates the favored positions of ions. Our VSFG results, combined with the results of electrochemical and electrokinetic experiments performed by our collaborators, suggest that the additional free volume in (*R*)-PC in comparison to racemic PC enables ions to penetrate the surface bilayer in the pure enantiomer at all electrolyte concentrations. In contrast, racemic PC follows a pattern similar to those of the other solvents discussed in this thesis. These results challenge how we typically think of the non-chirality-dependent physical properties of racemic and enantiomerically pure versions of the same material as being identical.

Taken together, the results presented in this dissertation underscore the need to improve upon the existing models of interfacial electrolyte solutions. This dissertation provides clear evidence that a more realistic and predictive model of interfacial electrolyte systems based on polar, aprotic organic liquids needs to include solvent structure and ionic volume.

Some of the immediate future directions for this project include performing electrolyte experiments for the EtCN/MeCN system, to help confirm the preferential partitioning of the solvents at the surface bilayer predicted by the molecular dynamics simulations. The simulations will also be extended to include different salts to study ion partitioning. It will also be important to study additional polar, aprotic organic solvents at the liquid–solid interface to develop a predictive understanding of the organization and ion partitioning in these systems. These experiments also demonstrate how ions can be used to probe liquid at interfaces. We intend to conduct experiments by change the cation and anions of the electrolyte to see how the bilayer responds to these changes.